Doctoral Dissertation
Doctoral Program in Metrology (34thcycle)

Metrology for Cultural Heritage: multispectral 3D models by photogrammetry

By

Leila Es Sebar
******

Supervisor(s):
Prof. Sabrina Grassini, Supervisor
Prof. Alessandro Re, Co-Supervisor

Doctoral Examination Committee:
Prof. Francesco Di Franco, Referee, Università dedli Studi di Palermo, Italy
Prof. Francesco Lamonaca, Referee, Università della Calabria, Italy
Prof. Lorenzo Ciani, Università degli Studi di Firenze, Italy
Prof. Anna Gueli, Università degli Studi di Catania, Italy
Prof. Guido Perrone, Politecnico di Torino, Italy

Politecnico di Torino
March 25th, 2022

Declaration

I hereby declare that, the contents and organization of this dissertation constitute my own original work and does not compromise in any way the rights of third parties, including those relating to the security of personal data.

<div align="right">

Leila Es Sebar

March 25th, 2022

</div>

I would like to dedicate this thesis to my beloved family

Acknowledgements

Abstract

This dissertation deals with the metrological validation of a digitalization approach that combines the use of photogrammetry and multispectral imaging (MSI) techniques in the field of Cultural Heritage.

Photogrammetry is a technique that is becoming more and more diffused for the creation of 3D realistic virtual replicas of historical artefacts since it allows the extraction of three-dimensional information about the geometry and overall appearance of an item from 2D digital images. On the other hand, MSI techniques are widely diffused, since they allow the detection and identification of the materials used by the artists based on their response to different wavelengths. It is worth noticing that, even if multispectral imaging can provide useful information with a non-invasive approach, it is usually employed as a two-dimensional technique.

Photogrammetry and multispectral imaging are often exploited for the study of historical artefacts but as separate tools. Nevertheless, the integration of data coming from MSI and photogrammetry can greatly increase the information within a 3D model, combining geometric and radiometric information and providing a powerful tool to the experts of the field. It is worth noticing that 3D models can be archived for posterity or shared among researchers, therefore avoiding the acquisition of wrong information from the dimensional point of view is of fundamental importance. However, there is no unique way to assess the dimensional accuracy of 3D models in the Cultural Heritage field.

To address these two issues, this dissertation presents a novel research methodology and experimental setup, that enable the acquisition of multispectral 3D models, combining the outcomes of photogrammetry and multispectral imaging in a single coordinate system. This approach has been developed together with a specific novel reference object, for application in the cultural heritage field. This has the main aim of being employed as a dimensional reference for the assessment of the dimensional

accuracy of 3D models. In addition, this item integrates several pictorial preparations, with materials historically employed on cultural heritage items, thus it can be used as a multispectral reference.

A metrological characterization of the proposed reference object has been carried out. First of all, a comparison among the information obtained through photogrammetry with different sets of data, collected by a Coordinate Measuring Machine and a laser scanner, is performed. These techniques measure the geometry of an object with different levels of uncertainty and therefore they can be used to assess the dimensional accuracy by inter-comparison. In addition, the influence that the selection of different wavelength ranges can have on the quality of a 3D model reconstruction is investigated. In particular, Infrared Reflected images, acquired within different ranges, are exploited for the construction of a 3D model, in place of traditional visible images. Eventually, the materials employed for the realization of the reference object have been characterized through portable Raman Spectroscopy.

In addition, an approach that enables the registration of both multispectral and geometrical data on a single virtual 3D model has been investigated. A 3D model from traditional visible reflected images is constructed, to extract geometrical information of an item. Subsequently, these pieces of information are stored and exploited to integrate textures obtained from several multispectral imaging techniques.

Eventually, the approach developed in this dissertation has then been used for the study of different case studies. In particular, some wooden sculptures from the Museo Egizio di Torino have been investigated, exploiting multispectral 3D models in support of the design of conservation treatments. In addition, photogrammetry has been used for the multi-analytical study of some bronze sculptures of a private art collection, the Collezione Gori at Fattoria di Celle.

Contents

List of Figures

List of Tables

Chapter 1

Introduction

1.1 Preface and Context

This dissertation presents a novel digitalization approach, which enables the creation of multispectral 3D models, based on the combined use of photogrammetry and multispectral imaging (MSI) techniques. A complete characterization of the presented methodology has been carried out, through a metrological and radiometric validation. Furthermore, this research presents the design and development of a reference object that can be used to assess the dimensional accuracy of 3D models obtained through photogrammetry and that can be employed as a reference for the integration of multispectral data on virtual replicas.

Even though digitalization techniques and 3D models of historical artefacts are becoming more and more widespread, there is a lack of knowledge regarding the assessment of the dimensional accuracy of these 3D virtual replicas in the Cultural Heritage field. Indeed, 3D models carry information regarding the geometry, colour, and texture of an item and they can be employed as a tool of documentation, to be shared among researchers and the public, or to create innovative museum exhibitions [5–7]. In addition, they can serve as an archive to preserve the artefacts for posterity, and safeguard them in case of loss. Taking into consideration all of these applications, it is important to assess the dimensional accuracy of a 3D model. Indeed, even if a virtual model could represent a photo-realistic replica of an object, it could carry incorrect information from the dimensional point of view.

Multispectral imaging techniques are commonly exploited for the analyses of artefacts, in order to support the decision-making process of conservators and curators. Indeed, these technologies allow the detection of materials on the basis of their response to radiation within different wavelength ranges. Although the great potential of the technique is commonly recognised and exploited, multispectral imaging is traditionally applied only on a two-dimensional level.

Techniques such as photogrammetry and multispectral imaging provide complementary information and they are usually separately performed on artefacts. In recent years, the possibility of integrating spatial and radiometric data on a unique model is arising great interest among the experts.

These two issues are addressed in this dissertation, which presents a novel reference object. This item has been designed and developed in order to have known features to be employed as a reference for the assessment of the dimensional accuracy of 3D models. Moreover, the novel reference object includes several pictorial preparations, with materials historically employed on cultural heritage items, arranged to be representative of cases that can be found in real artefacts. Therefore, the item can be used as a multispectral reference. In addition, the definition of an approach that allows the integration of these pieces of information in a unique 3D model is investigated and presented. The obtained multispectral 3D model allows navigating all different information in a single virtual replica, that, besides documentation, can carry also diagnostic data, within a single coordinate system.

The research work on the reference object has been carried out using two approaches, one regarding the metrological characterization and the other one dealing with the acquisition and integration of multispectral data.

The metrological characterization is performed by inter-comparing the data of the 3D model obtained through photogrammetry with different sets of reference data. These have been collected using different techniques that can measure the geometry of an object with different levels of uncertainty. In particular, measurements were acquired with a Coordinate Measuring Machine and a laser scanner, techniques that are often applied in the field of dimensional metrology [8]. Moreover, the influence of the selection of different wavelength ranges on the quality of a 3D model reconstruction is investigated. In particular, Infrared Reflected images, acquired within different ranges of the electromagnetic spectrum, are exploited for the construction

of a 3D model, in place of traditional visible images. Lastly, Raman spectroscopy has been applied to characterise the materials employed in the pictorial preparations.

To the aim of registering both multispectral and geometrical data on a single virtual 3D model, a novel approach has been investigated and presented. This involves the creation of a 3D model from visible reflected images, to obtain geometrical information. Then, textures obtained from several multispectral imaging techniques are integrated into the model itself.

At last, the proposed approach has then been exploited for the investigation of some case studies. In particular, some wooden sculptures from the Museo Egizio di Torino have been investigated, exploiting multispectral 3D models in support of the design of conservative treatments. In addition, photogrammetry has been used for the multi-analytical study of some bronze sculptures of a private art collection, the Collezione Gori at Fattoria di Celle.

1.2   Thesis Outline

In the following paragraphs, a summary of the structure of this thesis is presented.

Chapter 2 - This chapter presents an overview of the image-based techniques employed in the Cultural Heritage field, with a focus on photogrammetry and multispectral imaging.

Chapter 3 - This chapter depicts the novel reference object, which is the main subject of this dissertation. A description of its design and development is presented, with details regarding the techniques and materials employed.

Chapter 4 - This chapter presents the acquisition setup employed for the realization of multispectral 3D models. A detailed description of the components of the setup is provided, from the digital camera to sources and filters employed. To conclude the software and the novel strategy for integration of radiometric and geometrical data on a 3D model are described.

Chapter 5 - This chapter illustrates the 3D models obtained with the approach described in the previous chapters.

Chapter 6 - This chapter introduces the metrological characterization that has been carried out on the reference object, with a depiction of the different techniques employed.

Chapter 7 - This chapter presents the specific results regarding the multispectral imaging approach. A detailed description of each pictorial preparation present on the reference object is provided.

Chapter 8 - This chapter reports some case studies, regarding real historical artefacts on which the multispectral 3D imaging approach has been applied.

Chapter 9 - This chapter provides a resume of the results achieved with this research, with details on the main contributions and on the possible future work.

Chapter 2

Image-Based Techniques for Cultural Heritage

Among all the diagnostic techniques that are applied in the field of Cultural Heritage, image-based techniques are often exploited during the development of conservation treatments of the artefacts. Indeed, these tools can be of great support in the identification and characterization of the materials employed and they can provide insights on their structure and distribution on the artefacts, requiring no contact with the surface.

There is a wide variety of imaging techniques that can be employed, such as computed tomography [9], optical and electronic microscopy [10], or thermography [11]. In the group of non-invasive and non-destructive diagnostic tools, this dissertation is focused on the use of photogrammetry and multispectral imaging (MSI) techniques.

Some basic principles regarding Photogrammetry and multispectral imaging are presented in this chapter.

2.1   Photogrammetry for Digitalization of Cultural Heritage

2.1.1   Introduction

3D digital models are rich in potentiality useful for the cultural heritage field. As a matter of fact, a 3D model can be employed in all the processes of item preservation and conservation, as a tool for documentation and also monitoring its state of preservation. Moreover, it allows the storage of a reliable replica that can be shared with no limitation of time or space: having virtual access to cultural heritage items allows people to visit museums all over the world. A virtual reproduction of an artefact can be also employed for educational purposes. Eventually, a model can be also 3D printed, to create reliable replicas that can be exploited for innovative tactile exhibitions for disadvantaged users in museums [5–7].

Nowadays, it is possible to find a wide assortment of three-dimensional techniques that can be employed for the reconstruction of 3D models. The several techniques can be discriminated in actives, as laser scanners, and passives, based on the principle that they employ [12]. Photogrammetry falls within the passive techniques, since it is based on the acquisition and overlapping of multiple images, instead of scanning an item with an active structured strip of light [12, 13].

Photogrammetry is one of the most accessible and low-cost techniques for the digitalization of artefacts. Indeed, it is quite flexible and it can be performed using commercially available digital cameras. Photogrammetry can collect metric information about the geometry, shape, colour, and texture of an object, by identifying several homologous points among a set of digital images [12].

The term "photogrammetry" has been introduced by the German architect Meydenbauer, even though the first use of this technique dates back to 1849 by the military officer Frenchman Laussedat [14]. The technique was originally developed for studies in the architectural field and the creation of topographical maps [14], [15].

The principle that lay behind the photogrammetry techniques is collinearity. This establishes that a point of object space, its corresponding point on an image, and the projection centre of the camera, must lie on a straight line. The three-dimensional coordinates of a point, identified in at least two images, can be calculated

by the intersection of multiple rays of collinearity. This is called photogrammetric triangulation or bundle adjustment.

Nowadays, new approaches have been developed with respect to traditional photogrammetry, and extracting information from digital images is possible thanks to the development of progress on algorithms made within the computer vision field of research. In particular, 3D models can be created exploiting "Structure-from-Motion" (SfM), a self-calibrated approach that allows the extraction of both internal and external camera parameters through bundle adjustment, and "Multi View Stereo" (MVS), used for the detection of corresponding points between images [15–18].

2.1.2   Metrological aspects

The great availability of 3D scanning techniques made the process of creation of virtual replicas more accessible, even to not expert users. Indeed, a large variety of software is available, ranging from commercial ones to open source solutions. Photogrammetry software often provides a black box solution that allows obtaining a 3D model which presents a photo-realistic aspect. On the other hand, the results are not deeply investigated from the metrological point of view [19]. Indeed, several factors can affect the dimensional accuracy of 3D models and they must be further investigated. In some papers, a review of the principal factors that can influence the uncertainty of 3D imaging systems is presented and it includes issues such as the employed methodology, the ambient, the investigated materials, hardware, and software choices, and the influence of operators [20, 21].

Nowadays, even if several studies aim to investigate a shared solution for the uncertainty assessment of 3D models, there is a lack to be covered, related to suitable standards or the best practices to be employed [15, 20].

"Some publications have presented different test artifacts or new systems that could be used to test the performances of the photogrammetry approach [21, 22]. In some cases, the accuracy of a final model is determined by comparing the results with some reference data, acquired with active systems such as laser scanners [22–24]. Otherwise, the results are also evaluated on the basis of statistical parameters generated by the employed reconstruction software [25]" [26]. Therefore, it is possible to summarise the multiple ways in which the quality of a 3D model can be assessed in three main methodologies: the acquired dataset can be confronted

with techniques that provide a higher level of dimensional accuracy; an object of known shape and geometry can be employed as references; the virtual replica can be confronted with a model that is the results of the average on multiple acquisition [15, 19].

2.2   Multispectral Imaging Techniques for Cultural Heritage

Multispectral Imaging consists of the acquisition of images within a specific part of the electromagnetic spectrum when an item is illuminated with several radiations. This technique can be performed using common digital cameras, that have been modified in order to acquire a signal in a wide range of the electromagnetic spectrum, usually from 350 nm to 1100 nm.

The application of these techniques is of great interest to cultural heritage items because different radiations can be selected to investigate the surface of an artefact based on the aim of the diagnostic investigation. Indeed, the penetration power of certain radiation strictly depends on its wavelength, and therefore different radiations can be used to characterise the constituent materials and their distribution on the surface of the artefact. For instance, radiations with a long wavelength as IR can be used to investigate the presence of underdrawings on painted surfaces, because they are characterised by highly penetrative power.

In addition, it is important to underline that the radiation interacts with the material generating different results. In particular, the incoming radiation can be absorbed, reflected, or absorbed and then emitted as luminescence radiation with a longer wavelength [1], [27]. Therefore, taking into consideration the characteristics of the incoming and outgoing radiation, it is possible to investigate different features of the materials. In particular, it is possible to discriminate the MSI techniques based on the outgoing radiation that is acquired. The first category regards Reflected imaging, in which the incoming and outgoing radiations fall in the same range of the electromagnetic spectrum. Visible-reflected (VIS) imaging, Infrared-reflected (IRR) imaging, Ultraviolet-reflected (UVR) imaging, and False-colour reflected imaging are included in this group of techniques. The latter category is referred to Photo-Induced Luminescence imaging, in which the measured emitted radiation has
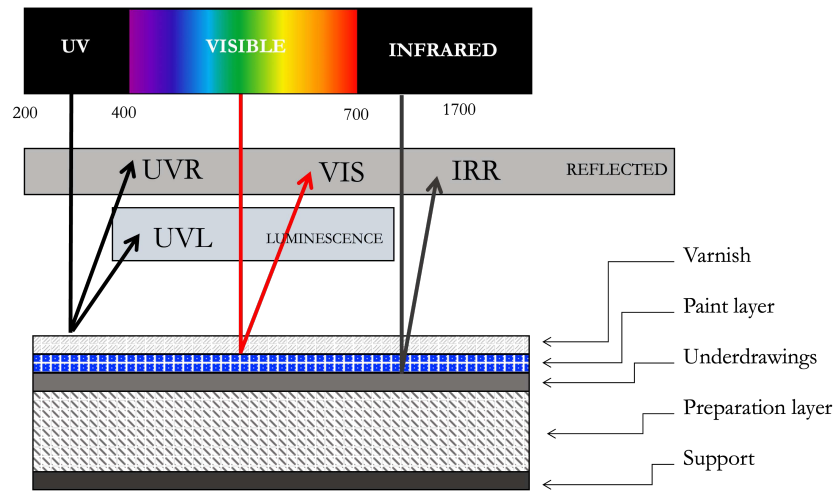
Fig. 2.1 Scheme of the Multispectral Imaging Techniques discussed in this dissertation. Details regarding the illumination conditions and the reflected/emitted radiation are summarised, with information about the penetration depth in the artefact. Figure adapted from [1].

a greater wavelength with respect to the incoming one. An example is ultraviolet-induced luminescence (UVL) imaging [1], [28].

In Figure 2.1 a scheme of the possible interaction between radiation-material and the generated signal is presented, with details on the penetration depth of the different wavelengths usually employed for diagnostic on artefacts.

In the following sections, the selection of MSI techniques that have been employed in this dissertation is presented.

2.2.1 Visible Reflected Imaging (VIS)

Visible-reflected Imaging is usually employed for the overall documentation of an item. In the field of cultural heritage, this technique is often applied in different steps. For instance, if an object is undergoing a conservative treatment, images are collected along with the applied treatments, namely before, during, and after [1, 28].

In VIS-reflected imaging, the object is irradiated with visible light and the signal is acquired in the visible region of the electromagnetic spectrum, i.e. between 400 nm and 780 nm.

2.2.2   Infrared Reflected Imaging (IRR)

Infrared-reflected (IRR) imaging technique is exploited in order to investigate details that are usually present on the preparation layer and that are not visible to the naked eye. For instance, some features that can be detected with this technique are preparatory drawings, regrets from the artist, or renovations [1, 29, 30].

To perform this technique, the item is illuminated with infrared radiation, and the reflected signal is collected in the infrared region of the electromagnetic spectrum, namely between 700 nm and 1100 nm.

2.2.3   UV-Reflected Images (UVR)

In this case, the artefact is illuminated with ultraviolet radiation, and the reflected signal is collected in the ultraviolet region of the electromagnetic spectrum, namely between 200 nm and 400 nm.

Ultraviolet radiation, characterized by short wavelengths, can be employed for the analysis of the external layers of painted surfaces. Indeed, materials such as varnishes, organic binders, and colourants can show luminescence properties [1, 31].

2.2.4   False-Colour Imaging

False-colour imaging is based on the combination and re-organization of the components of different images in order to obtain a final image, in which the colours do not correspond to the one that can be recognised by the human eye. Indeed some materials can assume a specific "false" colour, thus helping in the discrimination of features not detectable with other techniques.

The false colour processing can be applied using both images obtained with IRR or UVR techniques. Infrared Reflected False-Colour (IRR-FC) images are obtained by modifying the colour channels of a VIS-reflected image. In particular, the red and green components are inserted in the green and blue channels, respectively. Then the image obtained by IRR imaging is inserted in the red channel. Therefore, an image in which the reflected IR signal is represented by a red colour is created.

On the other hand, Ultraviolet Reflected False-Colour (UVR-FC) imaging is performed by inserting the UVR image in the blue channel of a VIS-reflected image and inserting its blue and green components into the green and red channels, respectively. In this way, in the final image, the UV radiation reflected by the material is represented by a blue colour [1, 28].

2.2.5   UV-induced Visible Luminescence Images (UVL)

Ultraviolet-induced luminescence (UVL) imaging is executed when an item is irradiated with ultraviolet radiation and the emitted signal from the material, i.e. luminescence, is acquired in the visible region of the electromagnetic spectrum $(200 - 400$ nm).

This technique is very useful for the identification of fluorescent material and also for the study of their distribution on the surface. Indeed this technique is often used also for the detection of past conservation treatments, in which modern material could have been used in place of the historical ones. In addition, it can be used also for the study of the degradation and ageing of the materials [32–34].

Chapter 3

The proposed reference object

This chapter presents the proposed reference object, which has the principal aim of being a dimensional reference for 3D reliefs by photogrammetry. Moreover, the object can be employed also for multispectral imaging applications.

The design and development of the reference object will be presented, together with all the material and techniques employed for its realization.

Some of the work described in this chapter has been previously published in [26].

3.1 Design and development

The object was realised to have two principal aims. First, the object is designed to be employed as a dimensional reference for the assessment of the 3D models that are obtained by means of photogrammetry-based techniques. Then, the object has to be employed also a reference for multispectral imaging techniques and to integrate multispectral data on the traditional 3D models obtained with visible reflected images.

To address these two specific issues, the reference object was designed as described in the following.

In order to be employed as a traceable to length reference, the object was designed with clean and sharp edges, in the shape of a dodecahedron, using FreeCAD [35], an open-source software. Then, the reference object was manufactured by means of a

3D printer (ProJet 2500 Plus printer by 3D Systems), using the VisiJet® M2R-GRY UV-curable resin. The obtained object has a regular surface with a homogenous grey colour. Therefore, in order to make the object suitable for photogrammetry, several details were added on the surface and edges of the object during the design. In particular, on each face, several holes are present in order to enumerate them, while ticks are present on the edges. All these features were added to be detectable by the SIFT algorithm, in order to match the images of the object.
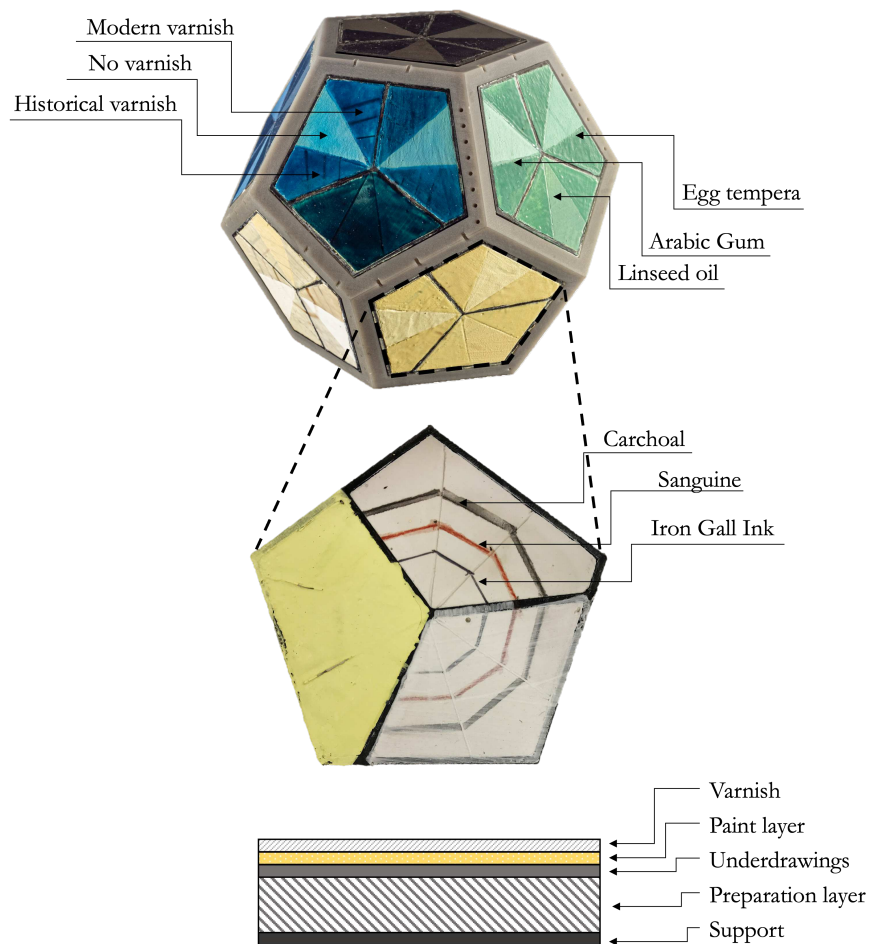
Fig. 3.1 Image of the reference object together with and scheme of the mock-up structure.

In each face, a pentagonal slot was realised, and each slot contain a mock-up with a specific pigment in combination with different materials. The aim is to create 12 different mock-ups that have the same structure as real artworks [36]. Therefore each one is composed of the following consecutive layers: support, preparation, underdrawing, pictorial layer, and varnishes.

Figure 3.1 illustrates the reference object, with details on the mock-up structure.

Each pentagonal mock-up was designed to contain a single pigment, in nine different combinations. Indeed each mock-up is divided into three sections, on the basis of the binder employed: linseed oil, Arabic gum, and egg tempera. Each section is further divided into three sub-sections, which are discriminated against based on the varnish employed. In particular, a historical varnish and a modern one were applied, and one sub-section was left uncoated.

A set of eleven pigments and one inorganic dye were selected for the realization of the mock-ups. The pigments are chosen to be representative of a wide historical period and they are provided by Kremer Pigmente GmbH Co. KG [37]. In particular, the pigments employed are lead white, white barium sulfate, bone black, magnetite black, Italian raw sienna, lead-tin yellow, minium, lac dye, azurite, malachite, verdigris, and lapis lazuli. Table 3.1 lists the employed materials for the pictorial preparations, including details regarding the preparation layer, underdrawing, binders, pigment, and varnishes. Each pigment is reported with a number and the Kremer Pigmente (Kr.) code.

The preparation layer is composed of *stucco*. In order to prepare this layer, a solution of animal glue and water was made, in a 1:14 ratio in weight. Then gypsum was added to this solution, till saturation was achieved.

On top of the *stucco* layer, with no distinction among the section and subsection, different signs that simulate the underdrawings were applied, namely Iron Gall ink, charcoal, and sanguine.

In order to realise the pictorial layer, each pigment/dye was ground in a mortar and then mixed with the selected binder till a homogenous texture was reached. The binders were selected to be representative of three artistic techniques and prepared as historically done for real artworks. In particular, the Arabic gum binder was prepared as a 1:10 in weight solution. The egg tempera binder was obtained as a mixture of

white vinegar and yolk (1:3 in volume). Finally, linseed oil was used without any pretreatment.

Finally, two different varnishes were applied on the pictorial layer, with a brush: a natural and historical varnish, namely mastic, and a modern acrilic one. A section was left uncoated. This is of particular interest for multispectral imaging applications, because varnishes can be detected thanks to UV wavelength. Figure 3.2 shows an intermediate stage of the preparation of the mock-ups, where it is possible to observe the preparation layers, the underdrawings, and the pictorial layer.

Table 3.1 Mock-ups composition of preparation layer, underdrawing, binders, pigment and varnishes. Each pigment is reported with a number and the Kremer Pigmente (Kr.) code.

Preparation Layer	Underdrawings	Binder	Pictorial Layer		Varnish
Gypsum	Chachoal	Egg tempera	Lead white	1, Kr. 46000	Historic terpene resin (mastic)
Animal glue	Sanguine	Arabic gum	White barium sulfate	2, Kr. 58700	Modern acrylic resin
	Iron Gall Ink	Linseed oil	Bone black	3, Kr. 47100	
			Magnetite black	4, Kr. 48800	
			Raw sienna italian	5, Kr. 40400	
			Lead-tin yellow light	6, Kr. 10100	
			Minium	7, Kr. 42500	
			Lac dye	8, Kr. 36020	
			Lapis lazuli sky-blue	9, Kr. 10562	
			Azurite natural fine	10, Kr. 10210	
			Verdigris syntethic	11, Kr. 44450	
			Malachite natural standard	12, Kr. 10300	
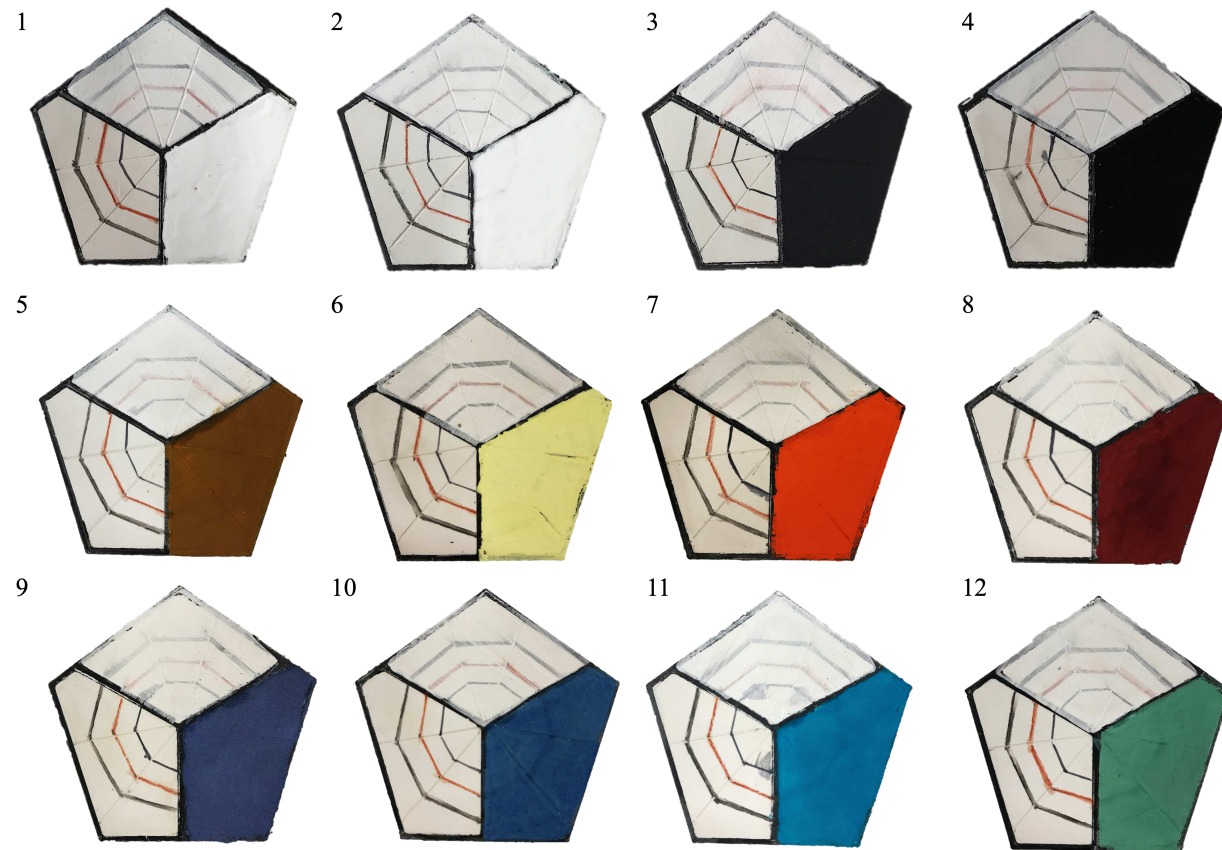
Fig. 3.2 Visible reflected images of mock-ups. The employed materials are reported in Table 3.1.

Chapter 4

Multispectral Photogrammetry Acquisition Setup

Some of the work described in this chapter has been previously published in [38], [2], [26].

4.1 Introduction

The setup was designed and realised during this research in order to create an automatized solution for the digitalization of artefacts from small to medium-size.

The system is based on a modular architecture, therefore it can be modified to satisfy different needs. In particular, the system is composed of a rotating platform, a dedicated control application, a digital camera, a set of filters to selected the desired wavelength range of the electromagnetic spectrum, and the radiation sources.

In this chapter, the setup employed to acquire the images is presented. In particular, the setup is composed of the following elements:

- rotating platform and dedicated control application, which allows acquiring images of artefacts at specific angles,

- modified digital camera, to collect the signal in a wide spectral range,

- radiation sources, to provide the desired radiation,

- filters, to select the desired wavelength range.

The above-mentioned components are described in the following sections.

4.2   Digital Camera

In order to integrate the data collected through Multispectral imaging on the 3D models obtained by means of Photogrammetry, it is necessary to employ a digital camera capable of acquiring radiation beyond the visible range.

A commercially available digital camera was specifically modified to this purpose by removing the IR-blocking hot mirror, in order to be sensitive in the range from 350 nm to 1100 nm.

In particular, the camera is a Fujifilm XT-30, coupled with an APS-C X-Trans 1 CMOS 4 sensor. In Table 4.1 all the specifications of the camera are reported.

The camera was equipped with a Minolta MC Rokkor-PF 50mm f/1.7 prime lens. In Table 4.2 all the specifications of the employed lens are listed.

During the images acquisition, all the parameters of the camera and lens must remain unchanged, in order to allow the photogrammetry software to recognize homologous features between images. To this aim, only prime lenses are employed, with manual focus.

The camera is mounted on a tripod during all the acquisition procedures in order to maintain the camera orientation fixed.

4.3   Radiation Sources and Optical Filters

In this section, the sources employed for each imaging technique are described, together with the specific optical filters necessary to select the appropriate signal to be measured. The filters were mounted on the employed lens.

In order to acquire visible-reflected images, a set of two incandescent light sources, namely tungsten-halogen lamps, was employed. In addition, a filter is required to block any radiation from the UV and IR region of the electromagnetic spectrum. Therefore, a visible bandpass filter, the HOYA UV&IR Cut, which selected

Table 4.1 Fujifilm XT-30 camera specifications

Fujifilm XT-30	
Image size (pixels)	4608 × 3072
Effective megapixels	26.1
Sensor size, type	23.5mm×15.6mm (APS-C) X-Trans CMOS 4 with primary color filter
Pixel size (μm)	4.94
ISO range	160–12800

Table 4.2 Minolta MC Rokkor-PF 50mm f/1.7 prime lens specifications

Minolta MC Rokkor-PF 50mm f/1.7	
Focal length	50 mm
Minimum aperture	f/1.7
Maximum aperture	f/16
Focus type	Manual
Type	Prime

the signal in the visible region (400-700 nm), together with a 455 nm long-pass filter, has been employed.

For the acquisition of UV-induced luminescence images, the above-mentioned filters were employed, together with two 365 nm LED lights (3000 mW AC/battery operated).

On the other hand, the same sources coupled with a 600 nm long pass filter, which blocks radiation in the visible and IR regions (400 - 1100 nm), with a transmission bandwidth of 60 nm (320-380 nm), were exploited to acquire UV reflected images.

The infrared reflected imaging technique was executed using two 850 nm battery-operated IR sources, and three different sets of filters: a 720 nm, an 850 nm, and 950 nm long pass filters, which block radiation in the UV and visible region (200 − 700 nm).

4.4 Rotating Platform and Dedicated Control Application

4.4.1 The Acquisition Setup

In order to reconstruct the 3D model of an artefact, it is necessary to acquire digital images of an object from different points of view and with a certain degree of overlap. In particular, for photogrammetric measurements, it is possible to acquire the images in two different configurations. The first one consists in maintaining the artefact in a fixed position and collecting images moving the camera around the item. On the other hand, it is possible to keep the camera position fixed and to place the item on a rotating platform. Then the item can be rotated by the desired angles, assuring the necessary degree of overlap between the images.

For this study, the second configuration is employed. In order to acquire the images of the artefacts understudy, a specific setup was developed.

"The setup includes an automatic photo-taking rotating platform and a control software application running on the computer together with the 3D reconstruction software. The main components of the system, shown in Fig. 4.1, are:

- A *rotating platform*, properly controlled by the system, which provides stable support for placing the artifact and acquiring photos at different views" [2] ©2021 IEEE.

- "A *stepper motor*, mechanically coupled to the rotating platform by means of a *reducing gearbox*, which is used to turn the rotating platform of the required angle. The gearbox reduces the angular velocity during platform rotation with the benefit of increasing the angular resolution. At the same time, the gearbox increases the available torque so that also artifacts weighting a few kilograms can be moved without affecting rotation accuracy. The authors employed a NEMA 17 motor and a 1:18 reducing gearbox, both allocated inside a 3D-printed enclosure, to provide a rotation resolution of 0.1 and a maximum error of 1, but other step motors can be used as well provided that they have suitable resolution and torque.

- A *motor driver* which is required to drive the step motor. Any driver can be used for this purpose. The authors employed a driver based on an A4988 chip, manufactured by Allegro MicroSystems. This driver, which has a very low cost, is used to drive the stepper motor by means of a simple digital interface for selecting both the rotation direction and the angular displacement. The driver is also able to control the motor current up to 2 A so that it is possible to employ a wide range of stepper motors and select the most appropriate torque.

- A *camera shot interface*, which allows the system to connect with the employed camera in order to take photos synchronously with the platform rotation. The interface technology changes, of course, with the selected camera" [2] ©2021 IEEE. For this setup, a Fujifilm XT-30 camera was employed. "Such camera provides a simple analog interface for triggering the focus and shot actions by means of two dedicated digital inputs with integrated pull-ups. Therefore, two open-drain buffers are included inside the camera interface to generate two positive edges over the two inputs with the required delays, so that the camera can complete the autofocus operation (if enabled) before taking the photo.

- A *control board*, which is based on the Arduino Uno development platform [39]. The Arduino Uno is programmed with firmware which is designed to control both the platform rotation and the photo shot triggering. The Arduino receives commands and configuration parameters from the processing computer over its USB Interface configured as a virtual serial port. All pictures are directly transferred to the PC from the camera, thus no manual intervention is required in this phase.

- A Linux-based *processing computer* running both the control application and the 3D reconstruction software. Among the available 3D reconstruction software, the authors selected Meshroom for this experimental setup because of its good performance and quite high flexibility. Since such software is open-source, this contributes to decrease the overall cost of the system and makes it possible to modify the software itself in order to fully integrate it with the acquisition system. Anyway, the proposed solution is easily configurable to work with other reconstruction software and different operative systems. No specific constraints are required in general for the computer. However, if the Meshroom software is used, a CUDA-compatible NVIDIA graphic card is required (level ≥ 2.0) [40]. In fact, Meshroom employs the graphics card

Fig. 4.1 "Block diagram of the proposed acquisition system. The digital camera and the processing computer can be selected accordingly the users' necessity" [2]. Figure from [2].

to create the 3D reconstruction and it can take advantage of the Cuda Parallel Computing Technology for decreasing the processing time and improving the 3D model quality. Of course, the higher are the performance of the computer the shorter is the reconstruction time for a given artifact, which may range from a few minutes to several hours. The computer requirements may differ if other types of reconstruction software are employed.

The camera is connected to the processing computer in order to transfer the acquired photos and process them. Most of the commercial cameras provide a standard USB interface and they are mounted by the Linux operative system as a *removable media* which can be accessed directly without the necessity of installing specific drivers or applications. This makes the photo transfer process quite straightforward for the control application independent from the specific model of camera employed in the setup." [2] ©2021 IEEE

4.4.2 Control Application

"A dedicated control application has been developed in the open-source Python Programming Language and wxPython with the aim of providing a user-friendly
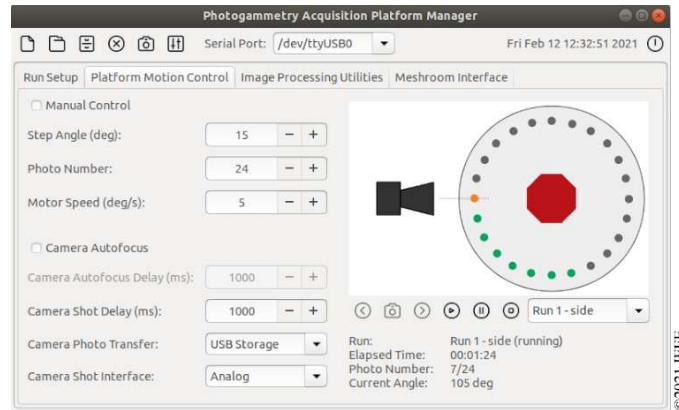
Fig. 4.2 "Grafical User Interface (GUI) of the proposed dedicated control application" [2]. Figure from [2].

Graphical User Interface (GUI) to configure the rotating platform and the photo transfer (Fig. 4.2). The application directly communicates with the control board in order to drive the platform, take the photos and, at the same time, it looks for the acquired photos in the camera folder, imports all the new ones and transfers them in the project directory. In this way, the reconstruction software can process the images, also in *live mode* during the photo-set acquisition.

The application, organized in several tabs, allows users to create and configure a reconstruction project on the processing computer. All the platform parameters, such as motor speed, number of steps, and shot delays can be configured from a dedicated tab." [2] ©2021 IEEE

4.5   3D model Reconstruction Software

"Meshroom [14], is based on the AliceVision Framework, and it was the selected software for the described experimental setup. This decision is due to the fact that it is a complete and open-source solution that allows one to perform all the photogrammetry pipeline and obtain a textured 3D model within a single application. It is also worth to notice that Meshroom has embedded a particular feature called live reconstruction. Such a function allows one to carry out an iterative reconstruction process: images can be added to the reconstruction process while they are acquired to augment the Structure-from-Motion (SfM) coverage. This way it is possible to

have a live result and to decide if more images are necessary to achieve complete coverage. In this way, it is possible to avoid the addition of redundant photos which would not improve model quality but would only increase computing time.

Meshroom has an embedded pipeline, that can be run without the necessity of manual intervention by the user, and can be configured and controlled by means of sockets or by a common command line. This way, the reconstruction process, and its configuration parameters can be partially controlled by the control application when necessary. The pipeline is created by connecting basic processing blocks together accordingly to the desired reconstruction steps. Optional processing blocks, including special filters, can be added when required by the specific application." [2] ©2021 IEEE

The pipeline is composed of several sequential steps:

- *Camera Initialization*, to import the images selected for reconstruction and load their EXIF metadata, namely date and time, and camera settings (orientation, aperture, shutter speed, focal length, ISO values).

- *Natural Feature Extraction*, to identify the groups of pixels (features) common to several images taken at different points of view. Typically, such a process employs the SIFT (Scale-Invariant Feature Transform) Algorithm, even though other algorithms are also available in Meshroom.

- *Image Matching*, to group all the images looking at the same areas of the artifact. This is performed taking into account the extracted features and comparing the image content for identifying all the images which share a specific part of the scene.

- *Features Matching*, to match the identified features to selected image pairs. For each image, the detected features are compared with the features of all other images, and a list of possible image pairs is computed. Subsequently, the most appropriate pair is selected by employing several possible metrics.

- *Structure from Motion (SfM) Creation*, to determine the geometrical placement and orientation (point of view) for each acquired image. This is carried out incrementally starting from two images and adding one image at a time by taking into account all image relationships determined in the previous steps.

- *Prepare Dense Scene*, to prepare the selected images for the Depth Map Estimation. This block undistorts each image and converts them to the EXR raster format.

- *Depth Map Estimation*, to compute the depth of each pixel in the images creating a so-called point cloud. The depth of each pixel in each image is statistically estimated by taking into account all information coming from the closest images and their orientation in the space. This is the most demanding processing in the 3D reconstruction pipeline. It is carried out for multiple pixels in parallel by taking advantage of CUDA and the high number of processing cores available on selected NVIDIA GPUs (Graphical Processing Units).

- *Depth Map Filtering*, to remove the statistical noise coming from the Depth Map Estimation.

- *Meshing*, to obtain the 3D structure of the artifact. This is carried out by joining all the Depth Maps in one single octree structure. Inside this structure, all estimated points are grouped and connected together until obtaining the faces of the artifact.

- *Meshing Filtering*, to clean up the rough mesh (i.e. collapsing too close vertices and too small faces).

- *Texturing*, to provide each face of the reconstructed model with the real appearance of the artifact (i.e. colours) [17].

Following the above-mentioned pipeline, it is possible to reconstruct a 3D model, starting from visible reflected images. A scheme of the default pipeline employed is shown in Figure 4.3a.

The same procedure could be employed also using the images collected with the other Multispectral Imaging techniques. It is worth noticing that this kind of approach leads to multiple and separate 3D models, which must be navigated and stored separately. In addition, their quality depends on the number of features that are detected by the SIFT algorithm, which are not necessarily the same for all the sets of images. For example, some sets of images could lead to a 3D reconstruction with a worse quality result than the one obtained with VIS-reflected images. For

instance, with UV-induced luminescence imaging, several parts of an item could have poor luminescence properties and therefore they could not be detected, leading to a less accurate result.

In order to overcome this issue, it is possible to exploit a Meshroom embedded feature. In particular, the software allows to re-texture a 3D model, using an additional set of images than the one employed for the creation of the point cloud and mesh from the visible reflected images. This is possible if the new images are acquired keeping the camera and item orientation and their position fixed during the acquisition. The process requires the duplication of the dense scene node, which is re-computed with the new set of images. Then, it is possible to generate a new additional texture. In Figure 4.3b it is possible to see how the additional nodes are connected to this aim. In this way, it is possible to re-texture the initial 3D model, obtained by visible-reflected images, and to integrate on it all the data collected with other multispectral imaging techniques, like UV-induced Visible Luminescence (UVL), Infrared-Reflected (IRR), UV-Reflected (UVR) imaging, Infrared-Reflected False-Colour (IRR-FC) imaging, and UV-Reflected False-Colour (UVR-FC) imaging.

Therefore, the procedure leads to the creation of a single 3D model on which the data coming from multiple MSI techniques can be mapped in only one coordinate system.
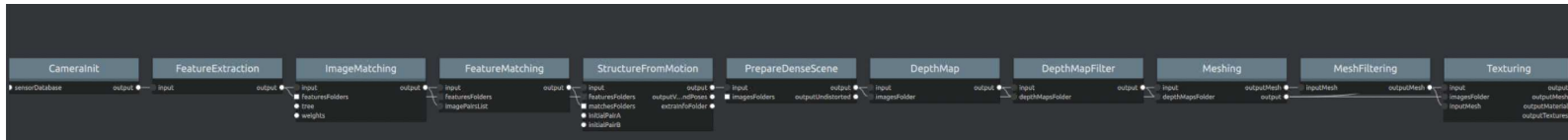
(a) Default pipeline used in Meshroom for the 3D model reconstruction.
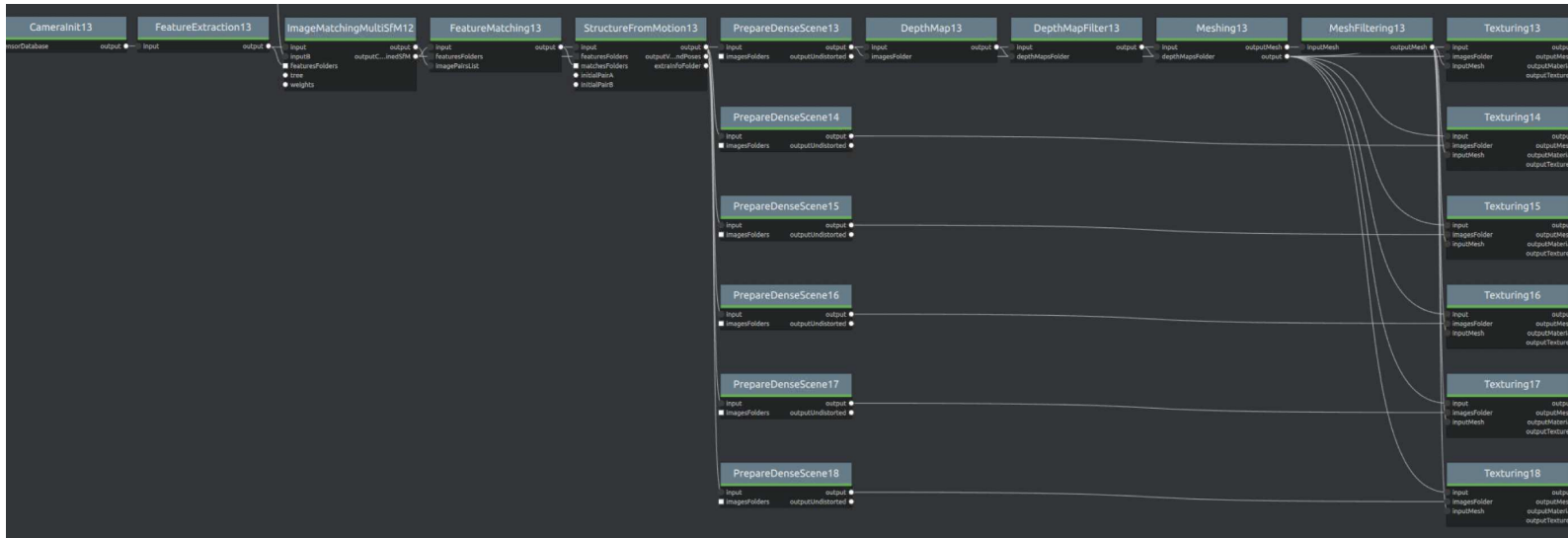
(b) Modified pipeline for the generation of the new texture.

Fig. 4.3 Pipeline used in Meshroom for the reconstruction of the 3D model with photogrammetry.

Multispectral Photogrammetry Acquisition Setup

Chapter 5

Multispectral 3D Model of the Reference Object by Photogrammetry

This chapter presents the result obtained from the reconstruction of the 3D model of the reference object by the combined use of multispectral imaging and photogrammetry. Indeed the final 3D model integrates information coming from several multispectral imaging techniques. In particular, the following techniques were employed: visible-reflected imaging, UV-induced Visible Luminescence (UVL) imaging, Infrared-Reflected (IRR) imaging, UV-Reflected (UVR) imaging. In addition, false colour image processing was employed to obtain Infrared-Reflected False Colour (IRR-FC) and UV-Reflected False Colour (UVR-FC) images.

The setup described in Chapter 4 was used to this aim. In Table 5.1 the parameters employed for the acquisition of the images are shown. The parameters have been kept constant during the measurements. The images were acquired placing the reference object in three different positions, in order to assure coverage of all the surfaces. The images were acquired with a step angle of 10°, for a total of 108 for each MSI imaging technique.

The default pipeline embedded in Meshroom was exploited to reconstruct the 3D model, as described in Section 4.5.

The result is presented in Figure 5.2. In particular, it is possible to observe the could point (Figure 5.1, 5.2a) obtained after the Structure From Motion step, in which the coordinates of the 3D points are extracted, together with the position of

Table 5.1 Parameters employed for the images acquisition.

Parameter	Value			
	VIS	**UVL**	**UVR**	**IRR**
Shutter Speed	1s	20s	20s	1/2s
Acquired images	108 (3x36)	108 (3x36)	108 (3x36)	108 (3x36)
ISO	200			
Image size	6240x4160			
Image Format	RAW			
Focal Lenght	50 mm			
Aperture	f/16			
Step Angle	10°			

the camera at the moment of the acquisition, forming three circles around the object. It is worth noticing that all the images were aligned (Figure 5.1).

The consequent step is the construction of a mesh, based on the SFM cloud, namely a continuous polygon surface (5.2b, 5.2c). The mesh has not a realistic colour, therefore the next step is to texture the mesh using the information coming from the digital images. The result is a textured 3D model, which is a virtual replica of the reference object (Figure 5.2d). The final 3D model is composed of a total of 378234 vertices and 756464 faces.

Once the mesh of the reference object has been constructed starting from the visible-reflected images, data coming from the MSI techniques employed were integrated. Following the procedure described in Section 4.5, it was possible to obtain a 3D model on which different textures were applied, within a unique coordinate system.

The result is presented in Figure 5.3. The model can be navigated as a single 3D file, in a similar way to what is traditionally done with 2D MSI imaging, creating multiple overlapping layers in a unique file in Photoshop, Gimp, etc.

This typology of a 3D model can be of great support for conservators and researchers since it allows to visualise the geometrical information and multispectral data immediately and easily. The correspondence among the multiple multispectral textures provides a better and deeper understanding, with respect to traditional 2D images, of the structure of an item, and on the distribution of the pigment, varnishes, and underdrawings on its surface.

Fig. 5.1 Point cloud obtained after the Structure from Motion step with camera positions, represented in white.

(a) Cloud point.

(b) Triangle mesh.

(c) Untextured Mesh.

(d) Textured 3D model.
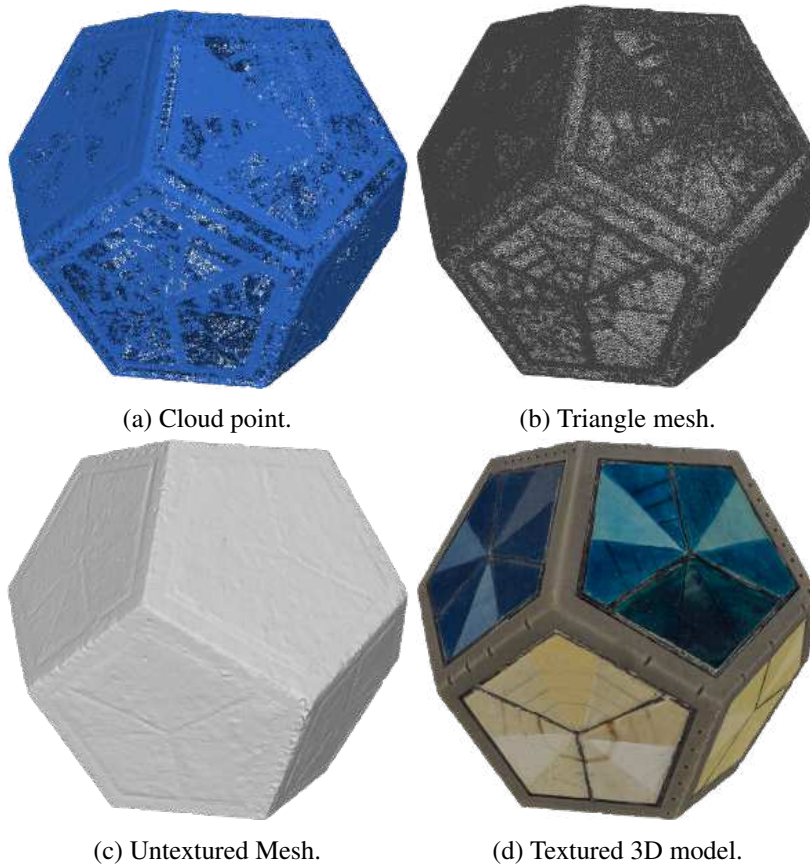
Fig. 5.2 Results of the several processing steps for the reconstruction of the 3D model of the reference object in Meshroom.

(a) VIS 3D model.

(b) UVL 3D model.

(c) UVR 3D model.
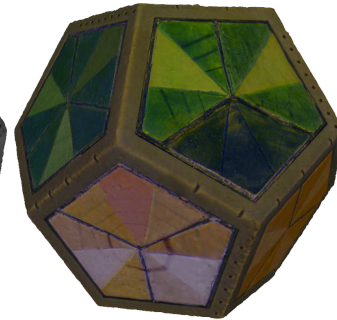
(d) UVR-FC 3D model.
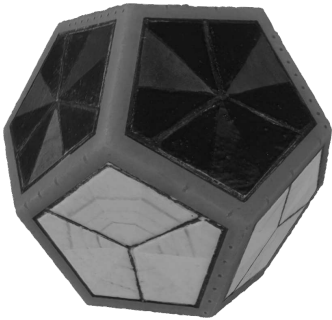
(e) IRR(720nm) 3D model.
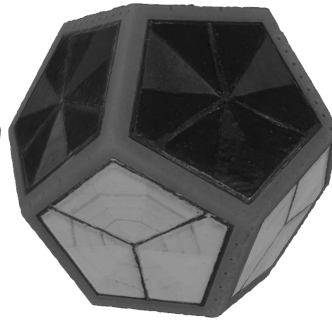
(f) IRR(850nm) 3D model.
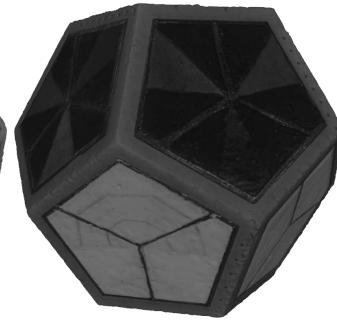
(g) IRR(950nm) 3D model.
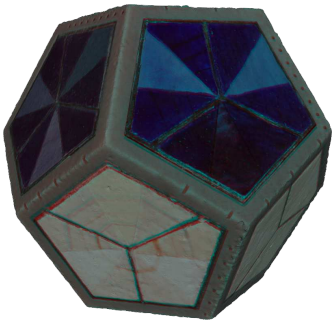
(h) IRR-FC(720nm) 3D model. (i) IRR-FC(850nm) 3D model. (j) IRR-FC(950nm) 3D model.
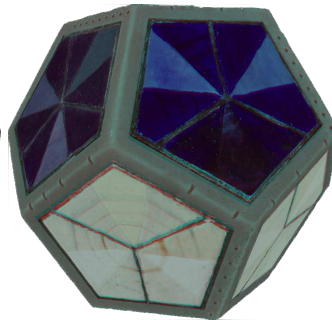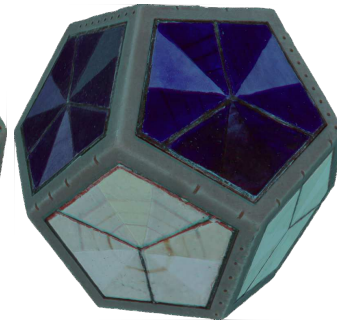
Fig. 5.3 Final 3D models of the reference object with integration of the Multispectral Imaging data.

It is worth noticing that no significant difference has been detected among the IRR models of the reference object obtained selecting different wavelength ranges, namely the 720 nm, 850 nm, and 950 nm long-pass filters. In particular, features such as the underdrawings were detectable in a comparable manner on all the IRR models.

Chapter 6

Metrological Characterization

Some of the work described in this chapter has been previously published in [3].

6.1   Introduction

One of the main aims of this research is to validate the accuracy of the 3D model obtained employing photogrammetry on the reference object presented in Chapter 5. To this aim, the results obtained through photogrammetry are compared with different sets of data. In particular, the reference object was measured by means of a Coordinate Measuring Machine (CMM), and a laser scanner. These techniques allow to measure the geometry of an object with different levels of uncertainty, and the obtained results are used as reference data set for inter-comparison.

Moreover, the influence of the different wavelength ranges on the quality of a 3D model reconstruction is investigated. In particular, Infrared Reflected images acquired within different ranges are exploited for the construction of a 3D model, in place of traditional visible images. Lastly, Raman spectroscopy has been applied to characterise the materials employed in the pictorial preparations.

This chapter presents these techniques and the achieved results.

6.2 Coordinate Measurement Machine

A Coordinate Measuring Machine is capable of measuring the geometry and form of an item by touching its surface with a mechanical tip, with very high accuracy. Then, the response of the probe is monitored and its position is recorded in the coordinate space as displacement from a reference point [41].

A contact CMM has been used to provide a traceable reference dataset for inter-comparison with the data collected by means of photogrammetry. In particular, the CMM exploited for this dissertation is the PMM-C 12.10.7 produced by Leitz and it is placed at the Istituto Nazionale di Ricerca Metrologica (INRIM, Turin, Italy).

In this case, the probing system was composed of three styli in a $90°$ configuration, each mounting a ruby sphere with a nominal diameter of 5 mm. This allowed reaching the surfaces of all the faces of the reference object, by moving the probing system along the X, Y, and Z axes. Prior to the acquisition of the measurements, each stylus is calibrated employing a reference ceramic sphere, whose dimensions are known. The reference object was glued on metallic support and then mounted on the workpiece table, to keep its position fixed during the data acquisition. In Figure 6.1 the employed setup is shown. In particular, it is possible to see the CMM machine together with the reference object, the probing system, and the reference ceramic sphere.

The CMM data were acquired and processed as described in the following. Ten points were measured in each face of the dodecahedron, placing the probe along the face borders. Overall 120 raw points were acquired. Then, the best fitting plane was computed for each face, using a Python script. Afterward, in order to find the coordinates of the vertexes, the computed planes were intersected in groups of three. The length of each edge was then computed as distances between the vertexes. Figure 6.2 presents the dodecahedron obtained with the above-mentioned approach.

It is worth noticing that this approach involves indirect measurements of the ver-texes coordinates with a consequent increase in the related uncertainty. Nevertheless, it was applied considering the difficulty of measuring the vertices directly by contact with the probe.

It is important to underline that the measurement is performed touching the surface of the object, by applying a force that can lead to surface deformation, considering that the plastic resin of the object has poor mechanical properties,

(a) Front view.   (b) Lateral view.

Fig. 6.1 The Coordinate Measuring Machine together with the reference object, the probing system with three styli, and the reference ceramic sphere employed for calibration.
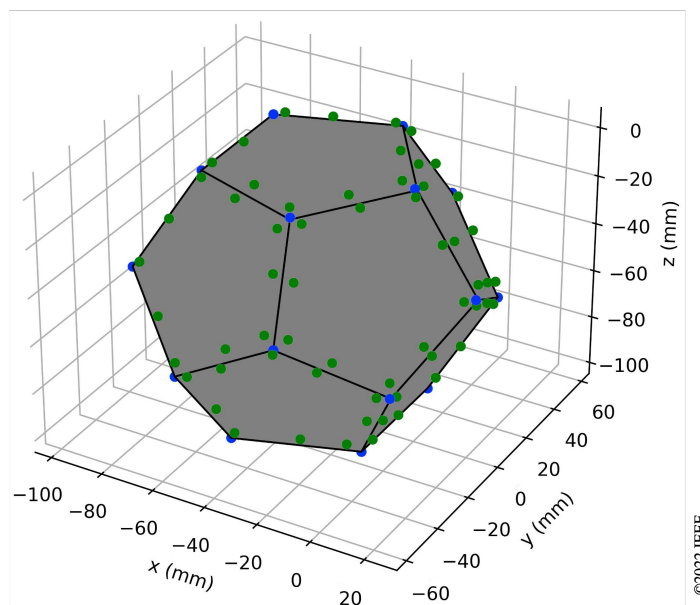
Fig. 6.2 "3D model of the reference object obtained by the Python script using the CMM measurements. The estimated dodecahedron vertices are in blue, while the raw points are in green" [3]. Figure from [3].

compared to metal or ceramic. Moreover, the resin thermal coefficient and the intrinsic 3D printer uncertainty must be taken into account for the estimation of the measurement uncertainty.

Therefore before the acquisition of all 120 raw points, several measurements were performed on the top plane. A standard deviation of the plane residual was computed to be in the order of 50 μm. This is the uncertainty level that is expected from the measurements, thus the uncertainty contribution of the CMM machine, which is in the micrometer scale as declared by the manufacturer, can be considered negligible.

The lengths of the same edges were measured also on the model obtained through photogrammetry (Chapter 5), as vertexes distances, with the open-source software Wings 3D [42]. The photogrammetric model was previously scaled, using the average edge length obtained with the CMM as reference. "In particular, the average edge length of the photogrammetric replica was calculated and the scaling factor was estimated according to the ratio L_{cmm}/L_{phg}, where L_{cmm} and L_{phg} are the average edge length from the CMM model and the photogrammetric replica, respectively" [3] ©2022 IEEE.

Table 6.1 reports the lengths of the edges obtained using the CMM and photogrammetry.

"From the data, it is clearly visible that all the edges, both from the CMM machine and the photogrammetric reconstruction, have lengths very close to the target design length of 44 mm. The two average lengths are almost equal as an indication of a proper scaling procedure. The standard deviation of the measurements obtained with the CMM machine is around 100 μm, as expected when considering the plane fitting residual. Even though the standard deviation of the measurement carried out over the photogrammetric model is about twice the one achieved by the CMM, such value is very promising and interesting also considering the cost of the respective instruments which is about 1500 USD for the photogrammetric setup and more than 225000 USD for the CMM equipment. Moreover, the maximum error between the lengths obtained from the CMM and the ones measured on the photogrammetric replica is about half a millimeter with a maximum relative error of about 1.3% (edge # 7) while the average relative error is around 0.4%, indicating that the employed photogrammetric approach leads to reliable results which are suitable in a wide range of applications and, in particular, in the cultural heritage field" [3] ©2021 IEEE.

Table 6.1 "Experimental data and results of the comparison between edge lengths of the reference object as obtained from the CMM machine and the edge lengths measured on the virtual replica obtained with the photogrammetric approach" [3] (PG). Table from [3].

Edge	CMM Length (mm)	PG Length (mm)	Error (mm)	Relative Error (%)
1	44.00	43.98	0.02	0.04%
2	43.86	43.98	-0.12	0.26%
3	43.94	44.31	-0.37	0.85%
4	43.93	43.78	0.15	0.34%
5	43.91	43.33	0.58	1.33%
6	43.99	43.96	0.03	0.06%
7	43.95	44.54	-0.59	1.35%
8	43.96	44.09	-0.13	0.28%
9	43.95	43.93	0.02	0.05%
10	43.94	43.87	0.08	0.18%
11	43.86	43.64	0.22	0.51%
12	43.89	43.81	0.08	0.19%
13	43.91	43.68	0.24	0.54%
14	43.92	43.98	-0.05	0.12%
15	43.85	43.62	0.22	0.51%
16	43.93	43.90	0.03	0.06%
17	43.82	43.62	0.20	0.45%
18	43.91	43.97	-0.07	0.15%
19	43.91	43.56	0.35	0.80%
20	43.88	43.90	-0.03	0.06%
21	43.66	43.99	-0.33	0.75%
22	43.55	43.70	-0.15	0.35%
23	43.64	44.03	-0.38	0.87%
24	43.80	43.98	-0.19	0.43%
25	43.78	44.08	-0.29	0.67%
26	43.92	44.06	-0.14	0.32%
27	43.94	43.53	0.41	0.94%
28	43.95	43.91	0.04	0.09%
29	43.91	43.79	0.12	0.27%
30	43.92	43.88	0.04	0.10%
Average	**43.88**	**43.88**	**~0.00**	—
Std	**0.10**	**0.23**	**0.25**	—
Max	—	—	**0.6**	**1.35%**

6.3   Laser Scanner

The laser scanner technology is widely applied in the Cultural Heritage field. It falls among the techniques that employ light to acquire three-dimensional information of an object. In particular, it is classified as an active technique, since light plays an active role in the measurement process. Indeed, a laser beam is used to reconstruct the three-dimensional geometry of an object without any contact with the surface [12], [43].

To perform a 3D relief of the reference object, a Konica Minolta Vivid 910 3D laser scanner has been used. This instrument is based on the principle of triangulation: the light-stripe method is used to emit a horizontal stripe of light, with a wavelength of 690 nm. The light is then reflected and collected by a CCD sensor and data are retrieved by triangulation. The object is scanned taking advantage of a Galvano mirror and this process is repeated multiple times till all the surface of the object is covered. This instrument is able to acquire up to up to 307 000 point cloud [43], [44].

In addition, this kind of laser scanner is also able to collect a colour image of an object through a CCD camera. The purpose of these measurements is to collect a set of reference data to assess the dimensional accuracy, therefore the texture obtained is not presented in this dissertation.

Different lenses can be mounted for the acquisition. In this case, the tele lens has been employed (f=25.5 mm), which allows reaching a resolution of about 50 μm as declared by the manufacturer. In Figure 6.3 an image of the Konica Minolta Vivid 910 3D laser scanner during the measurement is shown.

In Figure 6.4 the obtained result is presented. The 3D model has 674655 vertices and 1315980 faces. It can be noticed that the object's geometry and shape were successfully reconstructed, except for some details. This could be due to the fact that the varnished pictorial preparations have some reflective properties, that could have caused errors in the reconstruction.

The lengths of the 30 edges of the 3D model obtained with laser scanner were evaluated on the 3D mesh as distances between vertices with the open-source software Wings 3D [42]. Table 6.2 shows the data collected. In particular, the lengths of the edges obtained with the laser scanner are reported. Also, the one measured
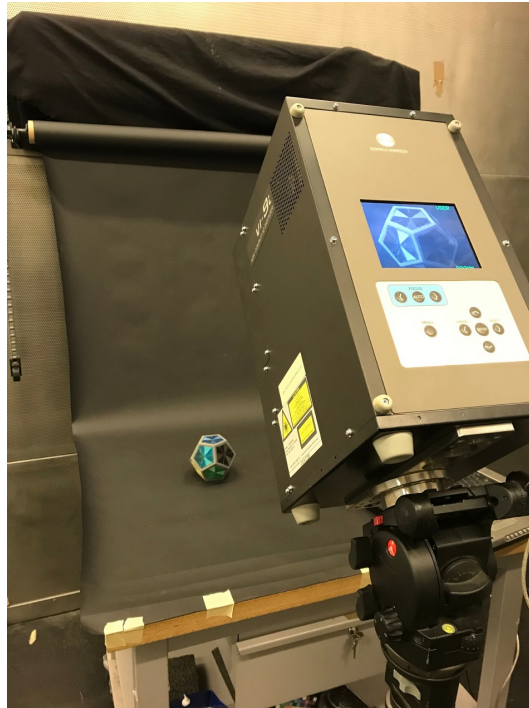
Fig. 6.3 Konica Minolta Vivid 910 3D laser scanner during the measurement together with the reference object.

on the model obtained through photogrammetry, with the methodology described in Section 6.2, are presented.

It is possible to deduce from the data that the lengths obtained with the two above-described methodologies, namely with the laser scanner and photogrammetry, are very close to the target design length of 44 mm, with an average difference of 48 μm. The standard deviation of the measurements acquired on the laser scanner model is about 400 μm. This value is about twice the one of the measurements performed on the photogrammetric model. In addition, the maximum error between the lengths obtained from the laser scanner and photogrammetry is 1.03 mm with a maximum relative error of about 2.38% (edge # 5).

These results can be explained by looking at the 3D model shown in Figure 6.4c, where is clearly visible that some features, like the edges, were not properly reconstructed. This is probably due to the fact that some faces of the reference object are reflective, because of the coating layer of varnish applied on the mock-up surfaces.

(a) Mesh of the reference object.   (b) Triangle mesh of the reference object.

(c) Textured mesh details of poorly reconstructed vertexes of the reference object.
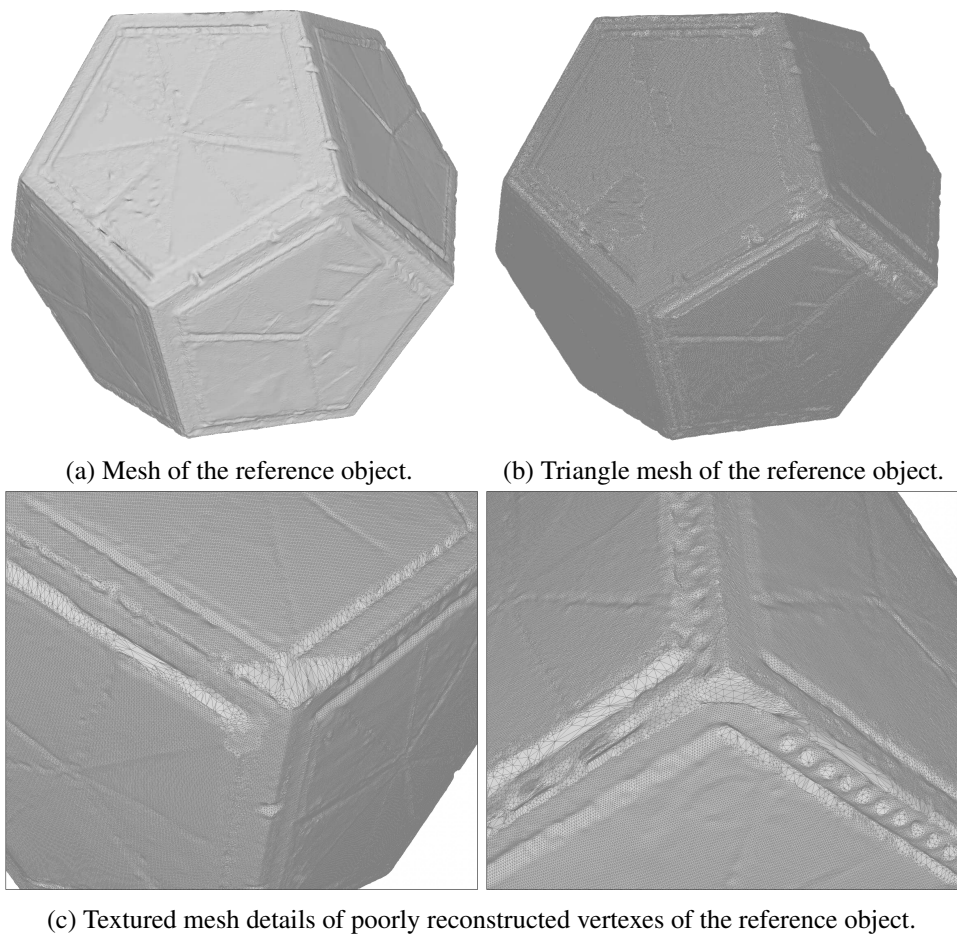
Fig. 6.4 3D model of the reference object obtained by means of the Konica Minolta Vivid 910 3D laser scanner.

Table 6.2 Experimental data and results of the comparison between lengths of the edges of the reference object as obtained from the Laser Scanner (LS) and the lengths of the edges measured on the virtual replica obtained with photogrammetry (PG).

Edge	LS Lenght (mm)	PG Lenght (mm)	PG-LS (mm)	Relative Error %
1	44.12	43.98	-0.14	0.32 %
2	43.33	43.98	0.66	1.49 %
3	44.01	44.31	0.30	0.67 %
4	44.27	43.78	-0.49	1.12 %
5	44.36	43.33	-1.03	2.38 %
6	43.70	43.96	0.26	0.60 %
7	44.85	44.54	-0.31	0.70 %
8	43.53	44.09	0.56	1.28 %
9	43.24	43.93	0.69	1.57 %
10	44.09	43.87	-0.22	0.51 %
11	43.99	43.64	-0.35	0.80 %
12	43.90	43.81	-0.09	0.20 %
13	43.74	43.68	-0.07	0.16 %
14	43.55	43.98	0.43	0.98 %
15	43.97	43.62	-0.35	0.80 %
16	43.61	43.90	0.30	0.67 %
17	43.52	43.62	0.10	0.24 %
18	43.98	43.97	-0.01	0.01 %
19	44.34	43.56	-0.78	1.80 %
20	43.95	43.90	-0.05	0.10 %
21	43.67	43.99	0.31	0.71 %
22	44.12	43.70	-0.42	0.96 %
23	43.15	44.03	0.87	1.99 %
24	43.68	43.98	0.31	0.70 %
25	43.93	44.08	0.14	0.32 %
26	43.22	44.06	0.83	1.89 %
27	44.38	43.53	-0.86	1.97 %
28	43.43	43.91	0.48	1.09 %
29	43.46	43.79	0.33	0.74 %
30	43.86	43.88	0.02	0.05 %
Avg	**43.83**	**43.88**	**0.05**	-
Std	**0.39**	**0.24**	**0.48**	-
Max	**44.85**	**44.54**	**1.03**	**2.38%**
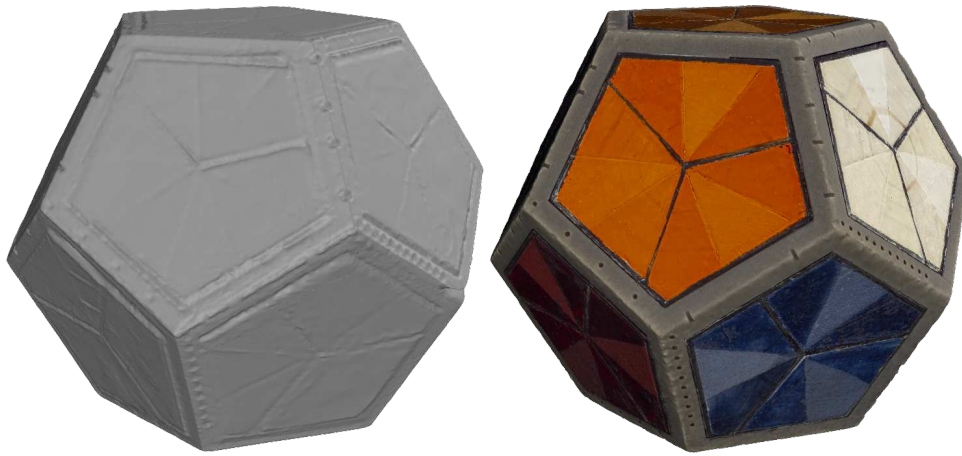
Fig. 6.5 3D model obtained by laser scanner (left) and by photogrammetry from VIS-reflected images (right).

Figure 6.5 illustrates the virtual replicas obtained with the laser scanner and photogrammetry.

Eventually, a further evaluation of the quality of the 3D model has been performed, comparing the visible light and the laser scanner virtual replicas. The comparison has been carried out with the software CloudCompare [45], an open-source processing software that allows computing distances between two meshes.

First of all, the two models were roughly aligned, selecting equivalent points on the surfaces and using the laser scanner model as a reference. The circles present on each face were used in this part of the process. Subsequently, the datasets were finely registered using the Iterative Closest Point (ICP) algorithm. This is able to minimize the difference between two entities in order to reach the best match to the reference dataset. This is an iterative process, that continues till a theoretical overlap of 100% is reached [45]. The iteration was concluded with an RMS (error difference between two iterations) value of 0.163938 (computed on 49976 points).

The obtained results are shown in Figure 6.6, as a colour-scaled map of the calculated distances, together with a graph that reports the probability density function of the calculated distances.

All distances are within the range between -0.913 mm and 1.093 mm, with a standard deviation value of 0.164 mm. The greatest positive discrepancies (red) are located along the edges of the model. These are the areas where the laser
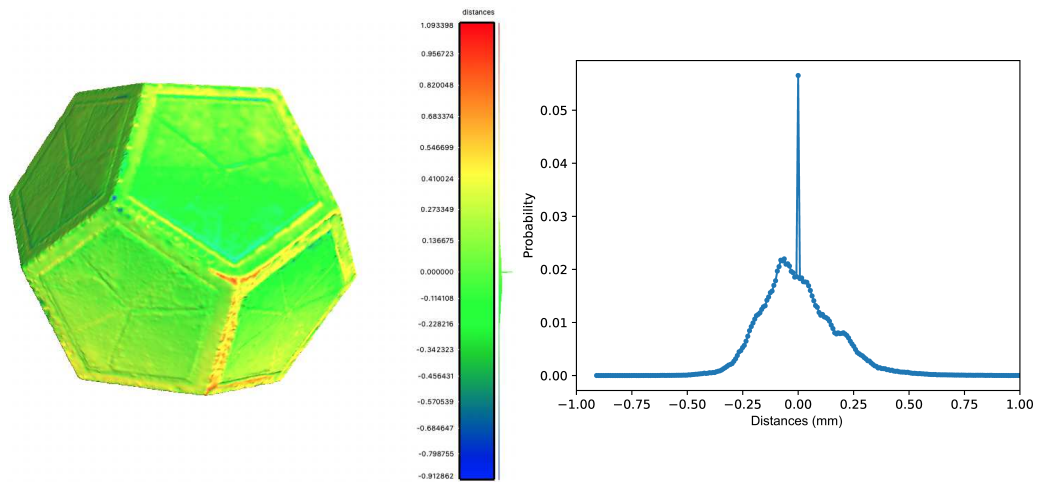
Fig. 6.6 On the left: mesh-to-mesh distances coloured map comparison of 3D model obtained with laser scanner and with photogrammetry from VIS-reflected images (colour scale in mm). On the right, the graph of the probability density function of the calculated distances is shown.

scanner failed to reconstruct some details because of the specular reflections, while photogrammetry was successful.

6.4   Influence of Wavelength

Infrared radiation presents a high penetrative power, and therefore it can not be absorbed by the most external layers that are usually present on the artefact surface. Indeed IR radiation can be exploited to detect concealed details, such as underdrawings or any features not detectable by visible light. This is possible because the organic materials used for colourants and varnishes, used to coat the surfaces of artefacts, are usually transparent to the IR radiation. In addition, also some pigments are transparent to such radiation, based on their composition.

Taking into consideration the highly penetrative power of IR radiation, it could be exploited to improve the 3D model creation. Indeed, using Infrared Reflected Images, instead of traditional visible reflected images, could decrease the reflections due to the shiny finishing of varnishes.

To this aim, this section investigates the use of IRR images for the construction of virtual replicas of the reference object. Three 3D models are reconstructed using IRR images acquired within three different IR wavelength ranges. In particular, three different sets of filters were mounted on the lens to select a specific region of the spectrum: a 720 nm, an 850 nm, and 950 nm long pass filters. The experimental setup described in Chapter 4 has been employed for the acquisition of the images and reconstruction of the virtual replicas.

The 3D models obtained with this approach are presented in Figure 6.7, together with the model reconstructed starting from VIS-reflected images. Compared to the VIS-3D model, the IRR-3D models present a more rough surface along the edges. On the other hand, all images were aligned, and the overall shape of the reference object was reconstructed.

(a) VIS.   (b) IRR - 720 nm.

(c) IRR - 850 nm.   (d) IRR - 950 nm.
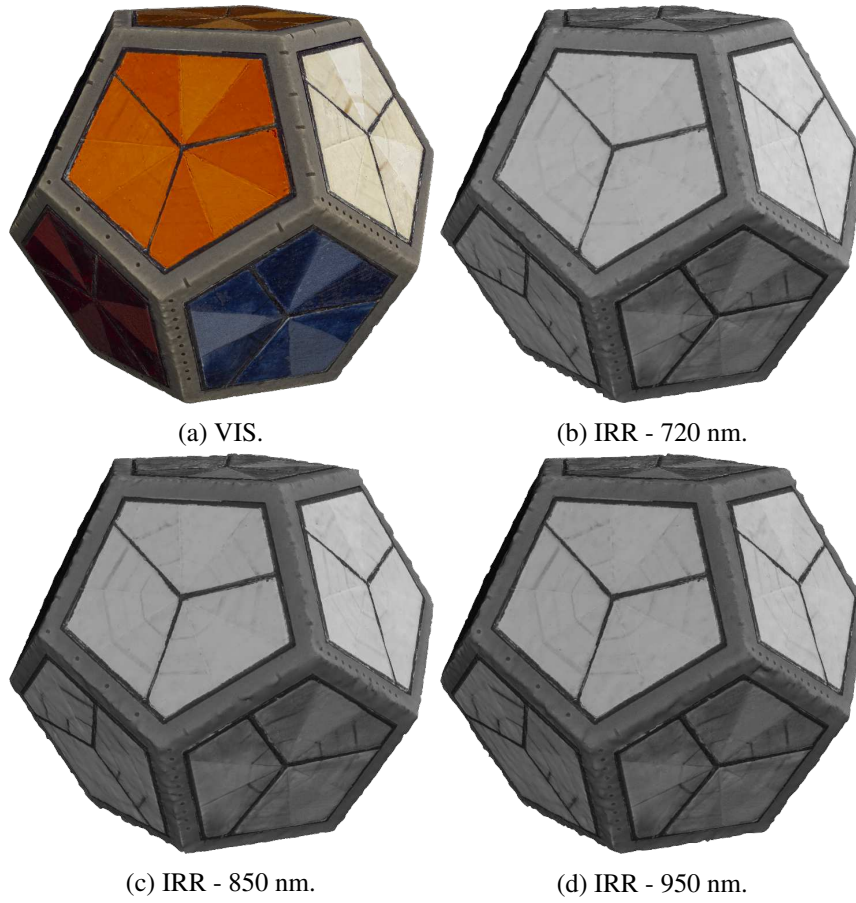
Fig. 6.7 Textured 3D models obtained from visible reflected images and from IRR images.

In order to evaluate the quality of the results, the VIS and the IRR virtual replicas were compared with the software CloudCompare [45].

Therefore the datasets were roughly aligned, selecting equivalent points on the surfaces and using the VIS model as reference. The circles present on each face were used as equivalent points. Then, the models were finely registered using the Iterative Closest Point (ICP) algorithm, which works in an iteratively way till the difference between two entities is minimised and a theoretical overlap of 100% is reached [45].

The obtained results are shown in Figure 6.6, as a coloured scaled map of the mesh-to-mesh calculated distances of the 3D models obtained from VIS and IRR images.

(a) VIS-IRR 720 nm.

(b) VIS-IRR 850 nm.

(c) VIS-IRR 950 nm.
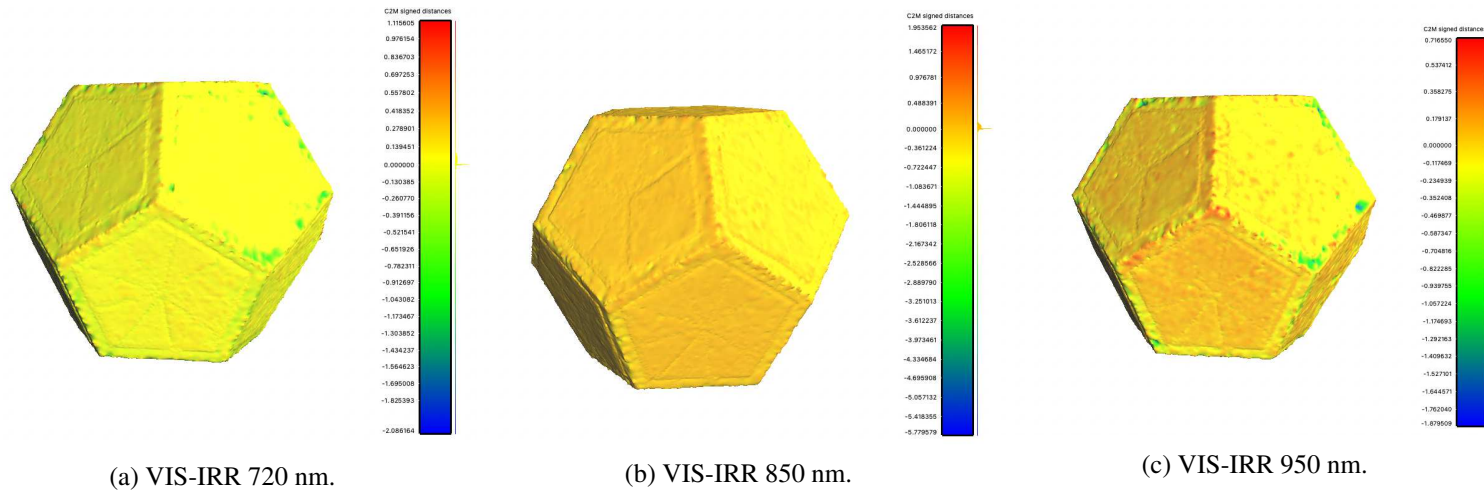
Fig. 6.8 Mesh-to-mesh distances coloured map comparison of 3D model obtained from VIS and IRR images (colour scale in mm).

Table 6.3 Values extracted from the mesh-to-mesh comparison. The RMS error of alignment is reported, together with minimum and maximum value of the distances and the extracted standard deviation.

	VIS-IRR 720 nm	VIS-IRR 850 nm	VIS-IRR 950 nm
RMS (mm) (computed on 50000 points)	0.109	0.194	0.140
Min. value (mm)	1.116	1.954	0.717
Max. value (mm)	-2.086	-5.780	-1.880
Standard Deviation (mm)	0.088	0.113	0.120

Table 6.3 lists the values extracted from the alignment of the meshes and the evaluation of the distances. In particular, the RMS error is reported, together with the minimum and maximum values of the distances and the extracted standard deviation. In addition, Figure 6.9 presents the probability density function of the calculated distances.

From Figure 6.9 it is possible to notice that the greatest majority of data falls in the interval close to zero, demonstrating that the photogrammetry procedure was successful. Notwithstanding, several discrepancies, both positive and negative, are located along the edges of the models. In particular, the model obtained with the 850 nm filter presents the greatest discrepancies, with a value of -5.780 mm (Table 6.3). From the data (Table 6.3) it is possible to state that the best result is obtained using the 720 nm filter, which leads to the smallest standard deviation value.

In conclusion, from the comparison, it is possible to state that using IRR images leads to the detection of fewer details with respect to the VIS images, resulting in virtual replicas with a greater number of surface irregularities, distributed along the edges.
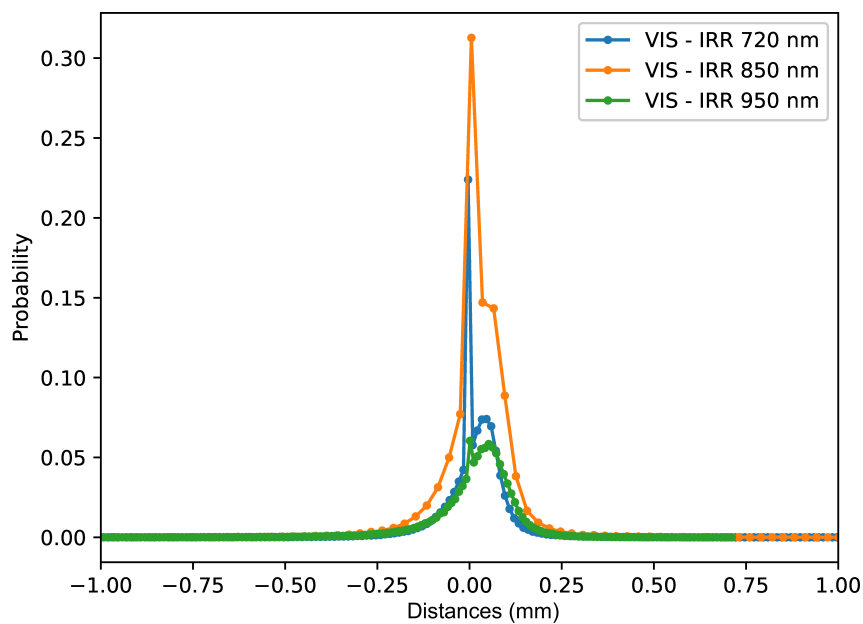
Fig. 6.9 Probability density function of the calculated distances among the VIS-3D model and the IRR-3D models.

6.5 Raman Spectroscopy

The set of pictorial preparation employed in the reference object has been characterized by means of Raman spectroscopy. This technique allows performing a chemical and mineralogical characterization of the employed materials.

As a matter of fact, Raman Spectroscopy has proven to be a powerful tool for the investigation and characterization of the materials usually employed in the Cultural Heritage field [4]. This technique is non-destructive and, with specific instrument configurations, can be performed directly on the artefact surfaces. Spectroscopic techniques allow to identify the chemical nature of a material and they are very useful for the identification of pigments and binders [46], [47], [48].

Raman Spectroscopy measurements were performed by means of two different Raman instruments, in order to exploit different laser wavelengths.

First, a BWTEK modular portable Raman spectrometer was employed. The instrument is provided of a monochromatic excitation laser, with a wavelength of 785 nm and a BTC675N spectrometer, that acquires the signal in the range between 65 cm^{-1} and 3350 cm^{-1}, with a resolution of 6 cm^{-1}. The instrument is equipped with a CCD sensor.

In addition, the portable i-Raman Plus (BWTEK) was employed. This instrument is furnished with a green excitation laser (532 nm), a BWS465-532S spectrometer that works within the range of $150 - 4200$ cm^{-1} and has a resolution of 7.3 cm^{-1}. The instrument is also equipped with a CCD sensor with a cooling system.

In order to acquire the spectra, the parameters, namely the laser power, the integration time, and the number of repetitions, were adjusted for each material to maximize the signal/noise ratio.

In particular, the laser wavelength was chosen based on the fluorescence response of the pigment-binder mixture. The laser power then was set to low values in order to avoid the modification of the mineralogical phases. Before every measurement session, calibration has been performed using a silicon wafer. Each spectrum was elaborated in Python in order to subtract the baseline, by means of asymmetric least square smoothing.

The measurements were performed directly on the surface of the pictorial preparations, using a non-invasive probe. The employed probe has a spot of about 90 μm.

The analyses were performed on each pigment-binder mixture, only on the uncoated surface, to avoid any fluorescence signal from the varnishes. Notwithstanding, the identification of the pigments was not always straightforward because the organic materials used as binders can lead to a fluorescence signal that can cover all the other vibrational modes.

The collected spectra for all twelve preparations are reported in Figure 6.10. Table 6.4 summarises the most relevant Raman vibrational modes identified for each pigment, together with the wavelength of the laser employed for the acquisition.

The two white pigments were successfully identified with the 785 nm laser. Lead white ($2PbCO_3 \cdot Pb(OH)_2$) spectra (Figure 6.10a) present peaks at 325, 413, 678, 969, 1050, 1372 cm^{-1} [47, 49]. On the other hand, the spectra of the white barium sulphate pigment, $BaSO_4$, show specific peaks at 454, 460, 988 cm^{-1} (Figure 6.10b).

The bone black pigment is produced with a process that involves the carbonization of bones in a range of temperature between 400°C and 800°C [37]. The relative spectra (Figure 6.10c), acquired using the laser with wavelength of 785 nm, present characteristic broad vibrational bands at 1331, 1594 cm^{-1}, as typical carbon-based black pigments [49, 50].

The Magnetite black pigment, with formula $FeO \cdot Fe_2O_3(Fe_3O_4)$, presents spectra (Figure 6.10d) with a strong vibration at 668 cm^{-1}. The spectrum was collected using the 785 nm laser.

Italian Raw Sienna pigment is a natural earth colour from Italy, which composition is $Fe_2O_3 \cdot nH_2O + Al_2O_3MnO_2 + SiO_2 \cdot H_2O$. In the spectra (Figure 6.10e), collected on this material by means of an excitation laser of 785 nm, it is possible to identify the following peaks: 255, 293, 395, 1096, 1202, 1274, 1549 cm^{-1} [49].

In the spectra of Lead tin yellow (Figure 6.10f), Pb_2SnO_4, [49], it is possible to detect peaks at 131, 198, 271, 290, 377, 454, 523, 615 cm^{-1} [47]. The pigment was investigated using the 785 nm laser.

Both red pigments have been analysed with the 785 nm excitation sources. The spectra of Minium pigment, with formula Pb_3O_4, present peaks at 121, 390, 550 cm^{-1} [51] (Figure 6.10g). On the other hand, Lac dye, a laccaic acid, has been identified from the peaks present at 247, 318, 372, 536, 566, 607, 884, 1006, 1291, 1322, 1418, 1476, 1615, 1693 cm^{-1} [52] (Figure 6.10h).

The acquisition of the spectrum on the Azurite pigment was not straightforward with either of the laser excitation sources (532 nm and 785 nm). Indeed, in both cases, the material generated a strong fluorescent signal and no significant peaks have been identified (Figure 6.10j).

All blue pigments were analysed using the 532 nm laser excitation source. Lapis lazuli pigment, known as ultramarine blues, is a sodium calcium aluminum silicate $(Na, Ca)_8[(SO_4, S, Cl)_2(AlSiO_4)_6]$. The spectra (Figure 6.10i) present several peaks and, among them, characteristic vibrational modes of this pigment have been identified: $548, 2452, 3000$ cm^{-1} [47, 49, 53].

Verdigris pigment is a copper (II) ethanoate, with formula $Cu(CH_3COO)_2$ [47], and has been identified by the peaks at 228, 318, 702, 945, 1418, 1442, 2939 cm^{-1} [54] (Figure 6.10k).

Malachite pigment is a natural basic copper carbonate, $2CuCO_3 \cdot Cu(OH)_2$ [37]. In the spectra (Figure 6.10l), a strong fluorescent signal is present, but it is possible to identify peaks at 110, 139, 174, 315, 399, 738, 940 cm^{-1} [47, 49].

Table 6.4 Identification of Raman vibrational modes on spectra acquired on the pictorial layers. The table reports the name of the pigment, the Kremer (Kr.) identification code, the laser wavelength, and the most relevant peaks.

Pictorial layer		Laser	Identified Raman vibrational modes (cm^{-1})
Lead white	1, Kr. 46000	785 nm	325, 413, 678, 969, 1050, 1372
White barium sulfate	2, Kr. 58700	785 nm	350, 454, 462, 992, 1145
Bone black	3, Kr. 47100	785 nm	1331, 1594
Magnetite black	4, Kr. 48800	785 nm	668
Raw sienna italian	5, Kr. 40400	785 nm	255, 293, 395, 1096, 1202, 1274, 1549
Lead-tin yellow light	6, Kr. 10100	785 nm	131, 198, 271, 290, 377, 454, 523, 615
Minium	7, Kr. 42500	785 nm	121, 390, 550
Lac dye	8, Kr. 36020	785 nm	247, 318, 372, 536, 566, 607, 884, 1006, 1291, 1322, 1418, 1476, 1615, 1693
Lapis lazuli sky-blue	9, Kr. 10562	785 nm	548, 2452, 3000
Azurite natural fine	10, Kr. 10210	532 nm	fluorescence
Verdigris syntethic	11, Kr. 44450	532 nm	228, 318, 702, 945, 1418, 1442, 2939
Malachite natural standard	12, Kr. 10300	532 nm	110, 139, 174, 315, 399, 738, 940
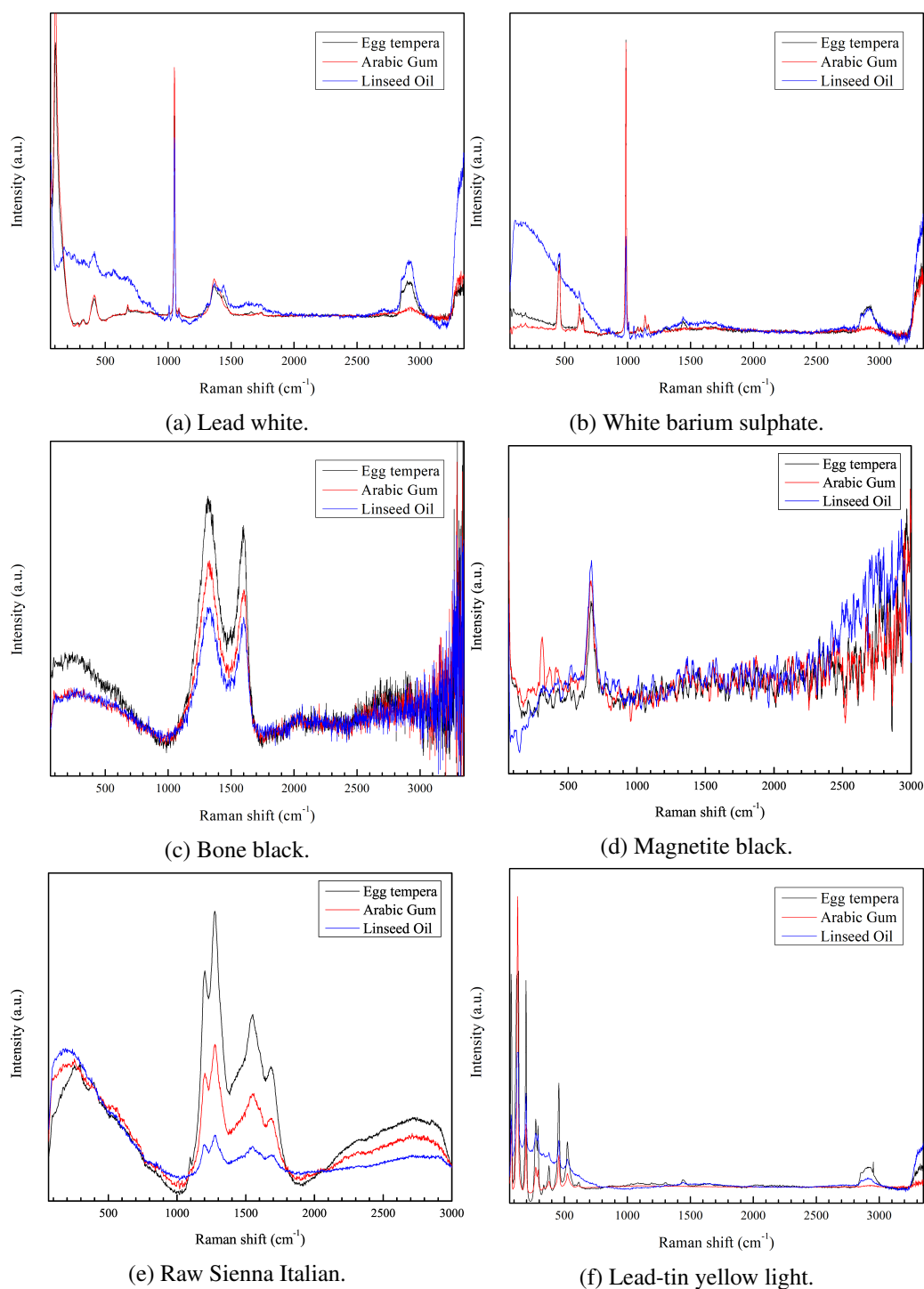
(a) Lead white.

(b) White barium sulphate.

(c) Bone black.

(d) Magnetite black.

(e) Raw Sienna Italian.

(f) Lead-tin yellow light.

Fig. 6.10 Raman spectra acquired on the uncoated surface of all mock-ups. A spectrum is reported for each pigment-binder mixture: egg tempera (black), arabic gum (red) and linseed oil (blue).

(g) Minium.

(h) Lac dye.

(i) Lapis lazuli sky-blue.

(j) Azurite natural fine.

(k) Verdigris synthetic.

(l) Malachite natural standard.
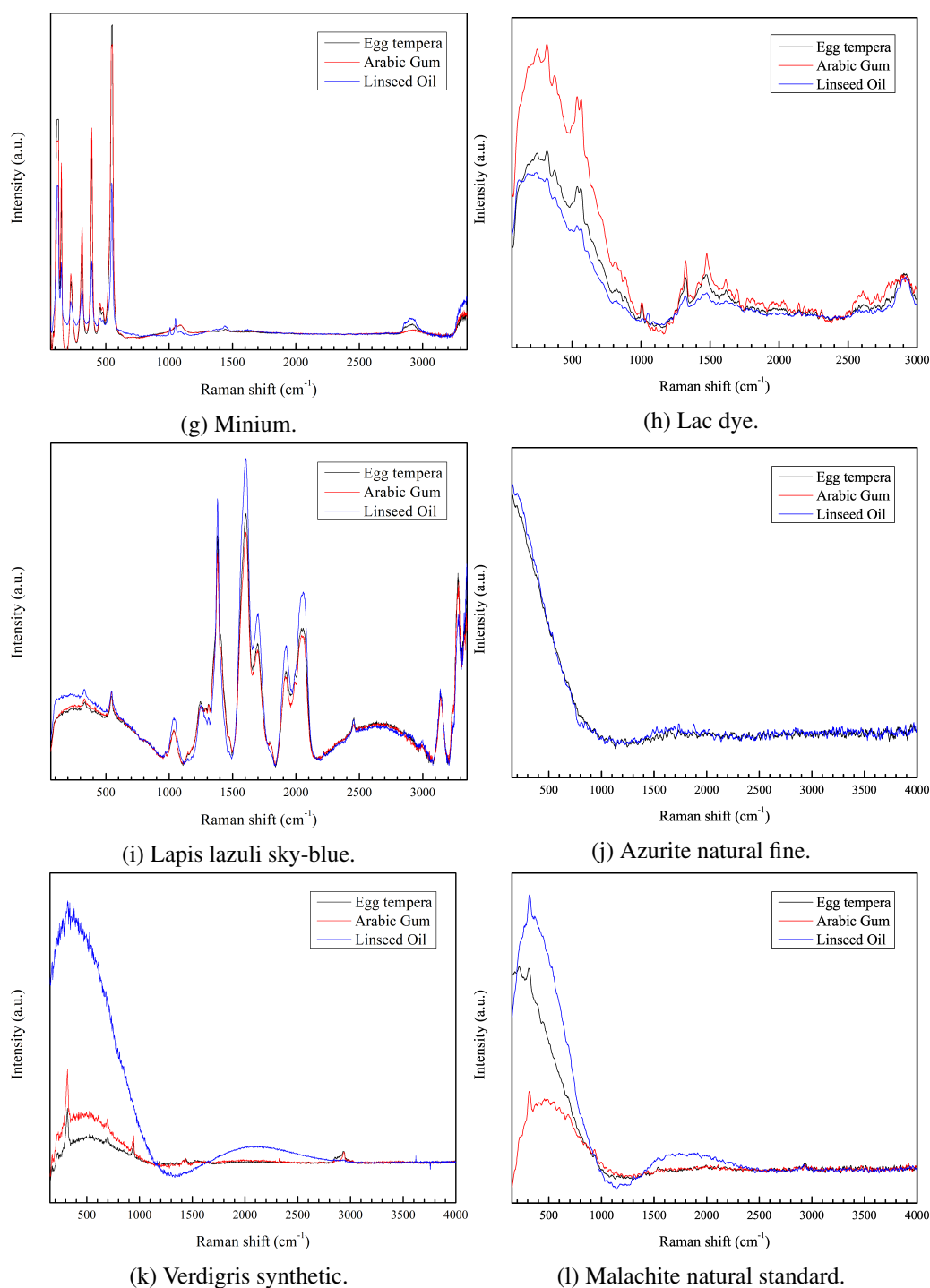
Fig. 6.10 Raman spectra acquired on the uncoated surface of all mock-ups. A spectrum is reported for each pigment-binder mixture: egg tempera (black), Arabic gum (red) and linseed oil (blue).

Chapter 7

Multispectral Imaging Approach

7.1 Introduction

In this chapter, the results of each multispectral imaging acquisition for all twelve mock-ups are reported. The images are obtained through several techniques, namely:

- Visible-reflected (VIS) imaging,

- UV-induced Visible Luminescence (UVL) imaging,

- Infrared-Reflected (IRR) imaging,

- UV-Reflected (UVR) imaging,

- Infrared-Reflected False Colour (IRR-FC) imaging,

- UV-Reflected False Colour (UVR-FC) imaging.

For the acquisition of all images, the experimental setup described in Chapter 4 has been employed.

From the results presented in Chapter 6, no significant difference has been detected among the filters (720 nm, 850 nm, 950 nm) employed for the Infrared Reflected images of the pictorial preparations. Therefore the results related to the use of the 720 nm filter are presented for sake of simplicity.

The specific features that have been identified using these techniques are presented and discussed in the following sections.

7.2   Pictorial preparations

7.2.1   Lead White

In Figure 7.1 results regarding the Lead white pigment are presented.

As can be seen in Figure 7.1b, the luminescence response of the pigment to UV radiation depends on the binder employed in the mixture. The pictorial preparation with egg tempera and linseed oil provides light blue colour, while the one with Arabic gum gives a dark-purple colour. On the basis of UV luminescence properties of the surface, it is also possible to distinguish among the varnished areas. In addition, with UVR imaging it is possible to discriminate more clearly the distribution of the historical and modern varnishes, that have a dark and light-grey appearance, respectively (Figure 7.1c). The underdrawings are slightly visible with IRR imaging since the material is slightly transparent to IR radiation (Figure 7.1d). Finally, the lead white pigment assume a light pink colour with UVR-FC (Figure 7.1e) and white in IRR-FC (Figure 7.1f) imaging.

(a) VIS   (b) UVL   (c) UVR

(d) IRR   (e) UVR-FC   (f) IRR-FC
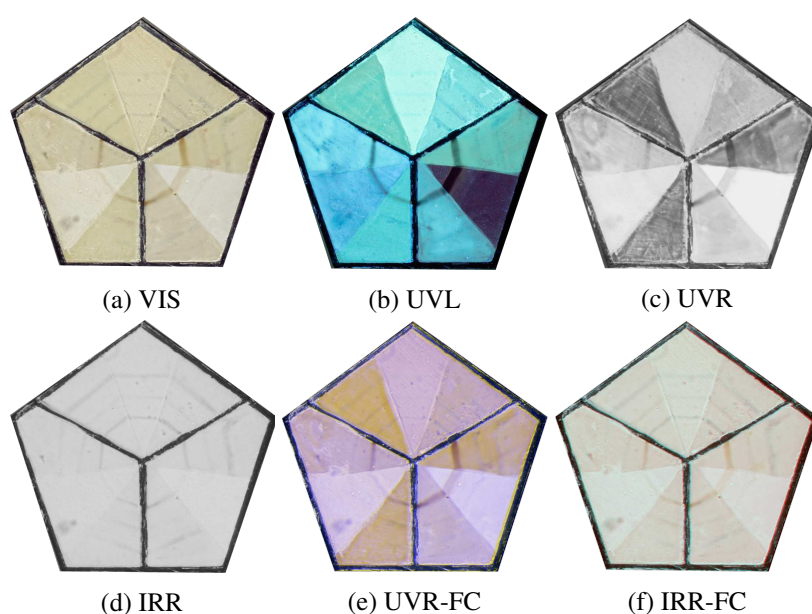
Fig. 7.1 Multispectral images of mock-up with Lead White.

(a) VIS   (b) UVL   (c) UVR

(d) IRR   (e) UVR-FC   (f) IRR-FC
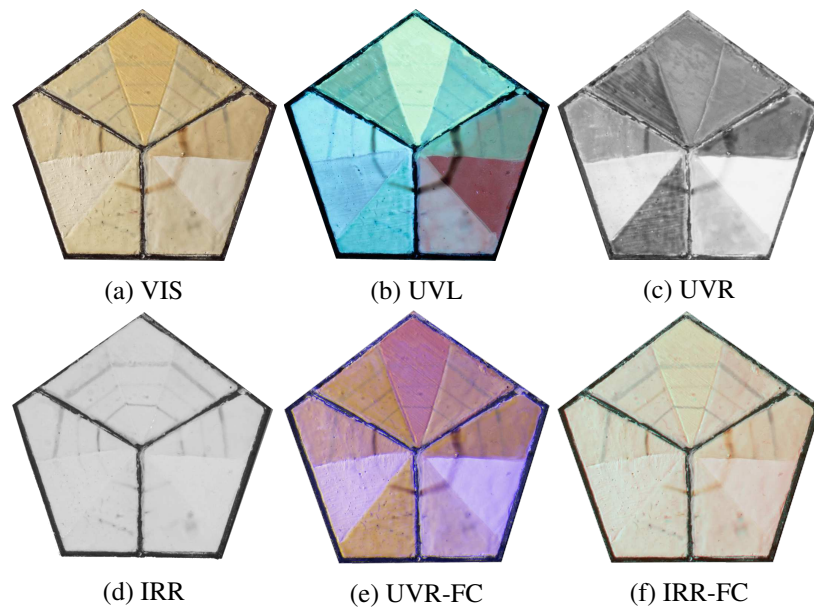
Fig. 7.2 Multispectral images of mock-up with White barium sulfate.

7.2.2 Barium sulphate

In Figure 7.2 results regarding the Barium sulphate white pigment are shown. It is possible to observe that the pigment provides a specific UV luminescence colour based on the binder employed. Indeed, for the mixture of the pigment with Arabic gum, egg tempera, and linseed oil the following colour response is obtained: pink, light blue, and light yellow, respectively (Figure 7.2b). In addition, the UVL imaging technique allows investigating the distribution of the varnish on the surface. As a matter of fact, the subsections with varnish assume a different colour with respect to the uncoated one. On the other hand, UVR imaging allows to discriminate in a clear way between the historical and modern varnish, that appear as dark and light-grey, respectively (Figure 7.2c). Moreover, Figure 7.2d shows that this pigment is transparent to the IR radiation and that all the materials employed for the realization of the underdrawing are detectable. Eventually, the lead white pigment assume a characteristic pink colour in UVR-FC (Figure 7.2e) and white in IRR-FC (Figure 7.2f).

(a) VIS   (b) UVL   (c) UVR

(d) IRR   (e) UVR-FC   (f) IRR-FC
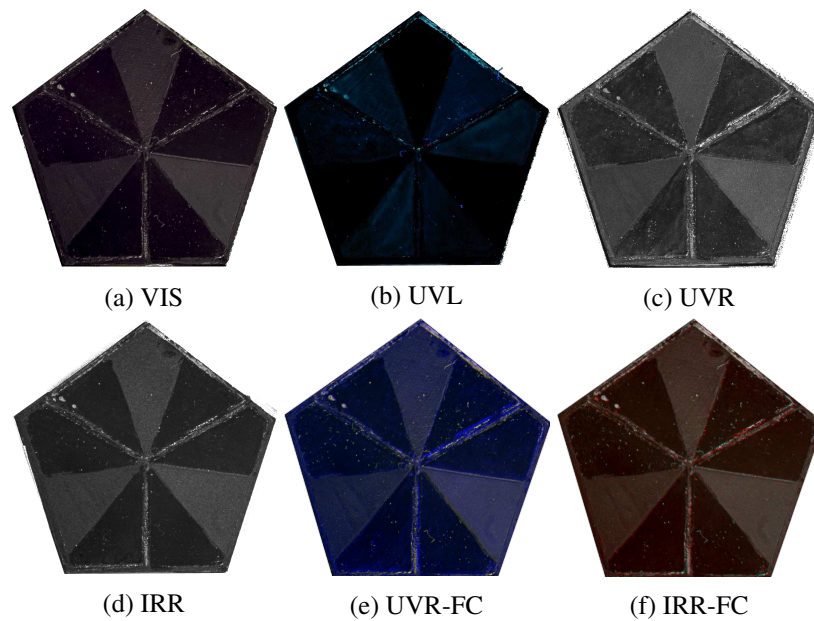
Fig. 7.3 Multispectral images of mock-up with Bone black.

7.2.3 Bone Black

MSI images acquired on the mock-up with bone black pigment are shown in Figure 7.3. This pigment, when uncoated has a dark luminescence response to UV radiation, and a slight blue luminescence when protected with varnishes (Figure 7.3b). UVR images (Figure 7.3c) confirm the results obtained with UVL imaging, and it is not possible to discriminate between the two typologies of varnishes employed. Bone black pigment is not transparent to IR radiation, indeed it is not possible to detect any of the underdrawings (Figure 7.3d). The pigment assumes a dark blue colour in UVR-FC images (Figure 7.3e) and a reddish dark colour in IRR-FC images (Figure 7.3f).

7.2.4 Magnetite Black

MSI images acquired on the mock-up with Magnetite pigment are shown in Figure 7.4. This pictorial preparation has a dark luminescence response to UV radiation, as shown in Figure 7.4b. UVR images allow discriminating between the coated and uncoated surfaces since varnishes have a dark response (Figure 7.4c). Magnetite pigment is not transparent to IR radiation, thus it is not possible to reveal the presence

(a) VIS   (b) UVL   (c) UVR

(d) IRR   (e) UVR-FC   (f) IRR-FC
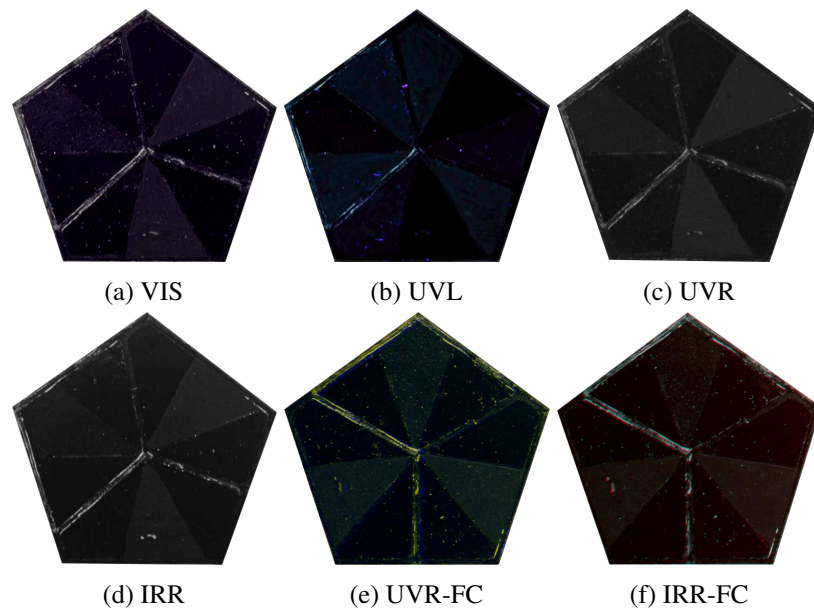
Fig. 7.4 Multispectral images of mock-up with Magnetite black.

of any underdrawing (Figure 7.4d). The pigment has a dark colour in the UVR-FC image (Figure 7.3e) and a reddish dark colour in IRR-FC image (Figure 7.3f).

7.2.5 Raw Sienna

Figure 7.5 presents the MSI images acquired on the mock-up with Italian raw sienna pigment. This pigment has a dark luminescence response to UV radiation, although the varnish coating is weakly detectable (Figure 7.5b). UV radiation is reflected in two different ways on the basis of the presence of varnish, which distribution on the surface is evident on UVR image (Figure 7.5c). The underdrawings are revealed in the IRR image in the varnished section with Arabic gum and egg tempera as binders. In addition, in the section in which linseed oil has been employed the brushstrokes are visible (Figure 7.5d). Raw sienna pigment acquires a characteristic purple colour in the UVR-FC image (Figure 7.5e) and a green-brown one in the IRR-FC image (Figure 7.5f).

7.2.6 Lead Tin yellow

In Figure 7.6 results regarding the Lead-tin yellow pigment are shown.

(a) VIS   (b) UVL   (c) UVR

(d) IRR   (e) UVR-FC   (f) IRR-FC
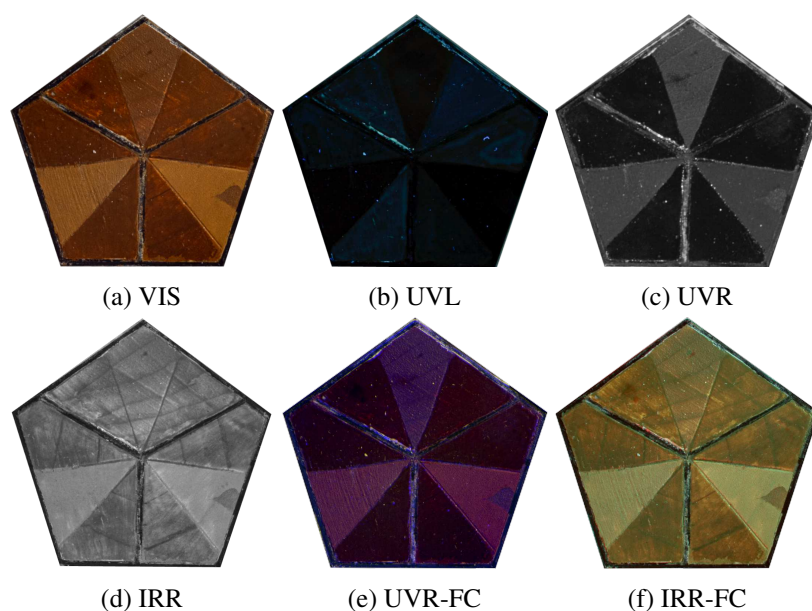
Fig. 7.5 Multispectral images of mock-up with Raw sienna italian.

It is possible to observe that the uncoated pigment provides a dark UV lumines-cence response, regardless of the binder employed. On the other hand, the varnishes are easily recognizable from a green luminescence colour, as shown in Figure 7.6b. Varnishes are recognizable from UVR imaging, having a dark response, but no difference is shown based on the varnish composition, as visible in Figure 7.6c. Underdrawings are visible in all the sections of the pictorial preparation in the IRR image (Figure 7.6d). It is interesting to notice that Lead-tin yellow pigment provides characteristic colours with false colour imagining processing. In particular an or-ange and white colours in UVR-FC (Figure 7.6e) and IRR-FC (Figure 7.6f) images, respectively.

7.2.7 Minium

In Figure 7.7 images obtained with MSI imaging on the Minium pigment are shown.

As can be seen in Figure 7.7b, the luminescence response of the pigment to UV radiation has no correlation with the binder employed in the mixture. On the basis of both UV luminescence and reflective properties of the surface it is possible to distinguish among the varnished areas (Figure 7.7b and Figure 7.7c). The under-drawings are slightly visible with IRR imaging, being the pigment transparent to IR

(a) VIS   (b) UVL   (c) UVR

(d) IRR   (e) UVR-FC   (f) IRR-FC
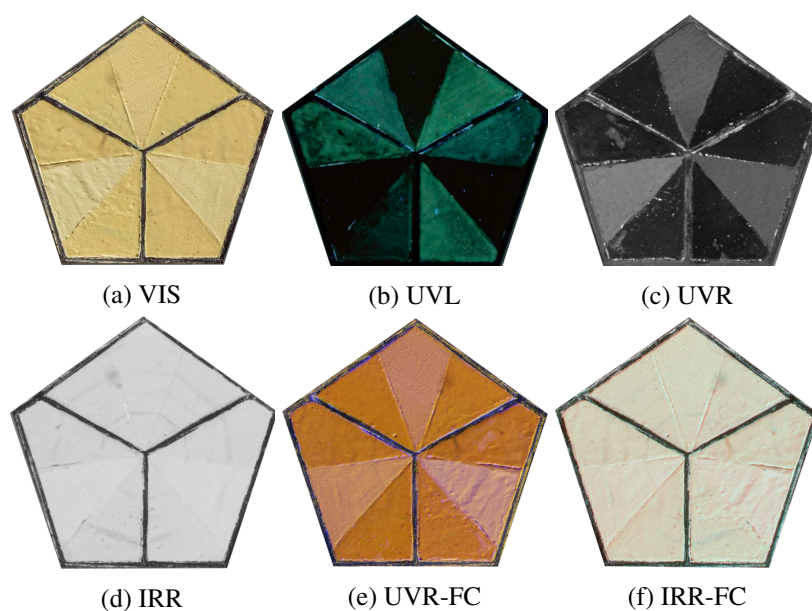
Fig. 7.6 Multispectral images of mock-up with Lead-tin yellow light.

radiation (Figure 7.7d). Eventually, the lead white pigment assumes a purple colour with UVR-FC (Figure 7.7e) and a yellow one in IRR-FC (Figure 7.7f) imaging.

7.2.8   Lac dye

In Figure 7.8 images obtained with MSI imaging on the Lack dye mock-up are shown.

Lac dye has poor luminescence properties, giving a dark UVL response, as can be observed in Figure 7.8b. Notwithstanding, its UV reflective properties allow to recognise the varnished surfaces, since the coated areas present a dark response (Figure 7.8c). This particular pigment is strongly transparent to IR radiation, indeed all the underdrawings are sharply visible in Figure 7.8d, regardless of the binder and varnish employed. Lastly, this pigment has characteristic false colour features, that allow easy identification. In particular, the Lac dye assume a blue colour with UVR-FC (Figure 7.8e) and an orange one in IRR-FC (Figure 7.8f) imaging.

(a) VIS   (b) UVL   (c) UVR

(d) IRR   (e) UVR-FC   (f) IRR-FC
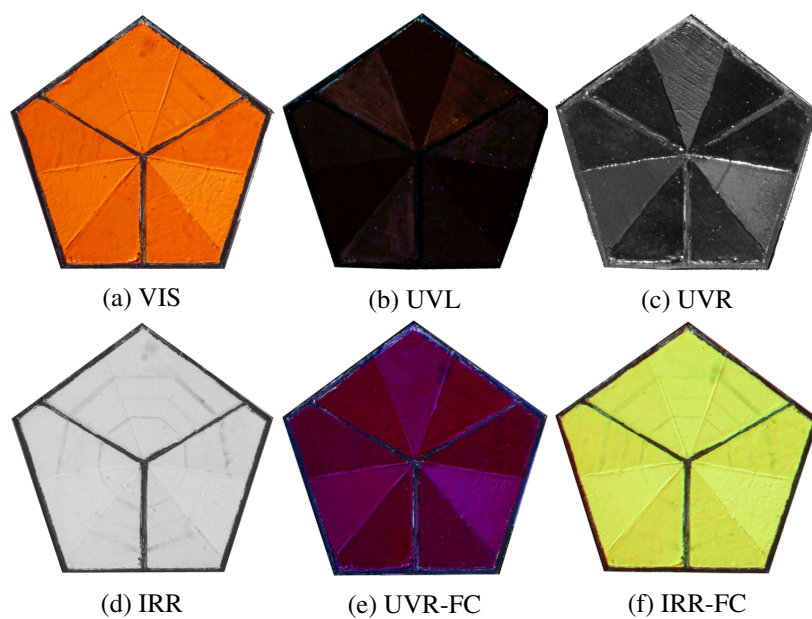
Fig. 7.7 Multispectral images of mock-up with Minium.

(a) VIS   (b) UVL   (c) UVR

(d) IRR   (e) UVR-FC   (f) IRR-FC
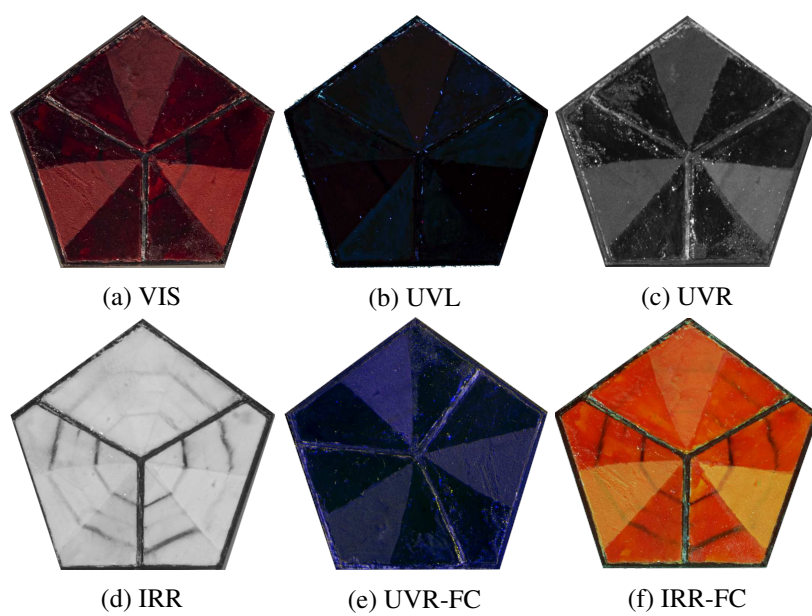
Fig. 7.8 Multispectral images of mock-up with Lac dye.

(a) VIS   (b) UVL   (c) UVR

(d) IRR   (e) UVR-FC   (f) IRR-FC
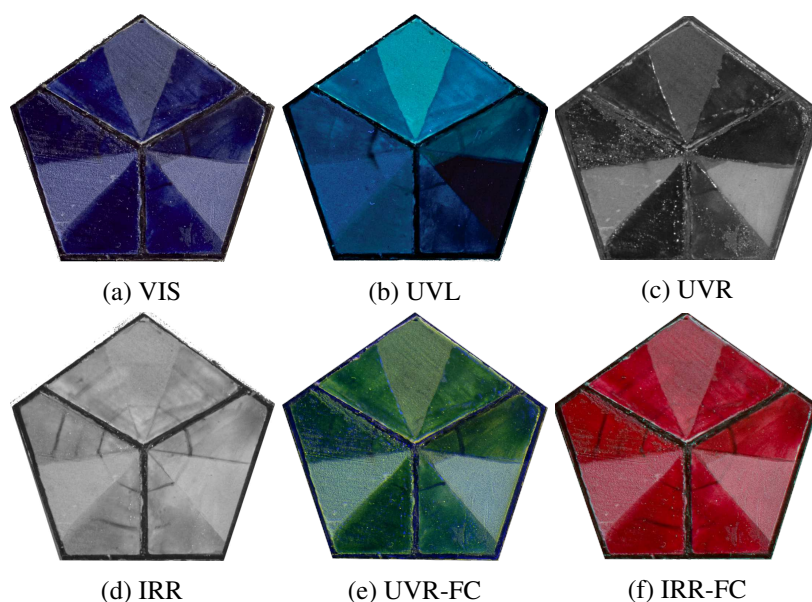
Fig. 7.9 Multispectral images of mock-up with Lapis lazuli sky-blue.

7.2.9 Lapis lazuli

In Figure 7.9 images obtained with MSI imaging on the Lapis lazuli mock-up are shown.

Lapis lazuli pigment presents a light blue luminescence when exposed to UV radiation (Figure 7.9b). It is worth noticing that the UVL response changes based on the binder. Actually, the uncoated Arabic gum binder gives a dark response, while the egg tempera and linseed oil have a light blue luminescence, even though in different shades. In the UVR image (Figure 7.9c) the distribution of the varnishes on the surface is distinguishable, as dark grey. The IRR image allows to visualize the underdrawings, most of all in the varnished sections, as shown in Figure 7.9d. Lapis lazuli pigment acquires characteristic colours after false colour image processing, as green in the UVR-FC image (Figure 7.9e) and red in the IRR-FC image (Figure 7.9f).

7.2.10 Azurite

In Figure 7.10 images obtained with MSI imaging on the Azurite mock-up are shown.

(a) VIS   (b) UVL   (c) UVR

(d) IRR   (e) UVR-FC   (f) IRR-FC
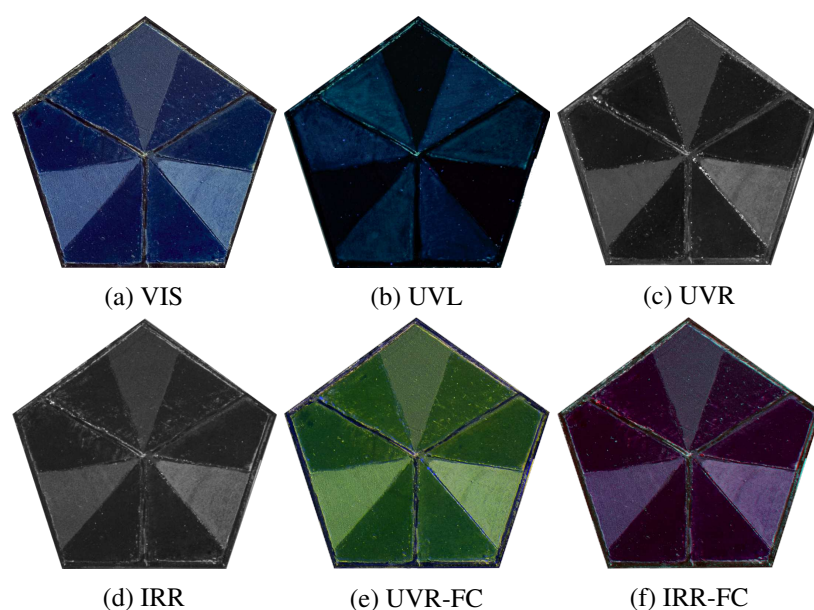
Fig. 7.10 Multispectral images of mock-up with Azurite natural fine.

Azurite pigment exhibits a dark blue luminescence when exposed to UV radiation (Figure 7.10b). It is possible to observe that both the UV luminescence and the UV reflected radiation allowed to map the distribution of the varnishes on the surface, as presented in Figure 7.10b and Figure 7.10c. No particular difference is detected among the different binders. The azurite pigment absorbs the IR radiation and therefore the underdrawings are not revealed with the IRR technique (Figure 7.10d). The Azurite pigment presents characteristic colours in false colour imaging. In particular, the pigment acquires a green colour in the UVR-FC image (Figure 7.10e) and a purple one in the IRR-FC image (Figure 7.10f).

7.2.11   Verdigris

In Figure 7.11 images obtained with MSI imaging on the Verdigris mock-up are shown.

The verdigris pigment shows a dark UV luminescence when is uncoated. On the other hand, it is possible to recognise the varnished parts by a blue luminescence signal (Figure 7.11b) and a dark response in UVR imaging (Figure 7.11c). No particular difference is detected among the different binders or varnishes employed.

(a) VIS   (b) UVL   (c) UVR

(d) IRR   (e) UVR-FC   (f) IRR-FC
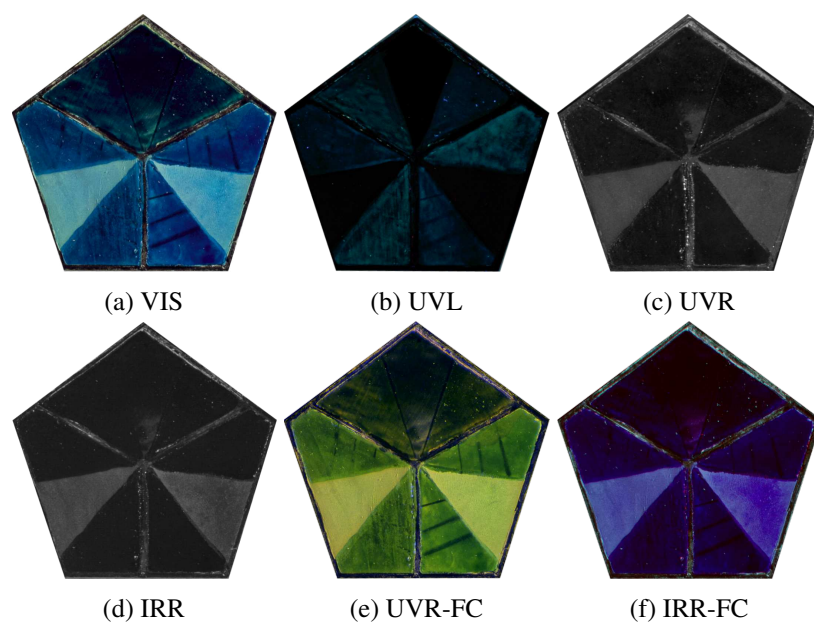
Fig. 7.11 Multispectral images of mock-up with Verdigris syntethic.

The underdrawings are not detectable in IRR imaging, since the pigment strongly absorbs the IR radiation (Figure 7.11d).

The Verdigris pigment presents a specific green colour in UVR-FC imaging (Figure 7.11e) and a dark purple one in IRR-FC imaging (Figure 7.11f).

7.2.12   Malachite

In Figure 7.12 images obtained with MSI imaging on the Malachite mock-up are shown.

It can be noted that the parts where the varnish is not present have a dark UV luminescence response, despite the combination of pigment and binder. It is possible to detect the varnish since they have a green luminescence colour (Figure 7.12b). In addition, the varnishes are recognizable also in the UVR image, having a dark response (Figure 7.12c). Underdrawings are not visible in all the sections of the pictorial preparation in the IRR image (Figure 7.12d). It is worth noticing that Malachite pigment provides specific colours with false colour imagining processing: light brown colour in UVR-FC image (Figure 7.12e) and light blue in IRR-FC image (Figure 7.6f).

(a) VIS   (b) UVL   (c) UVR

(d) IRR   (e) UVR-FC   (f) IRR-FC
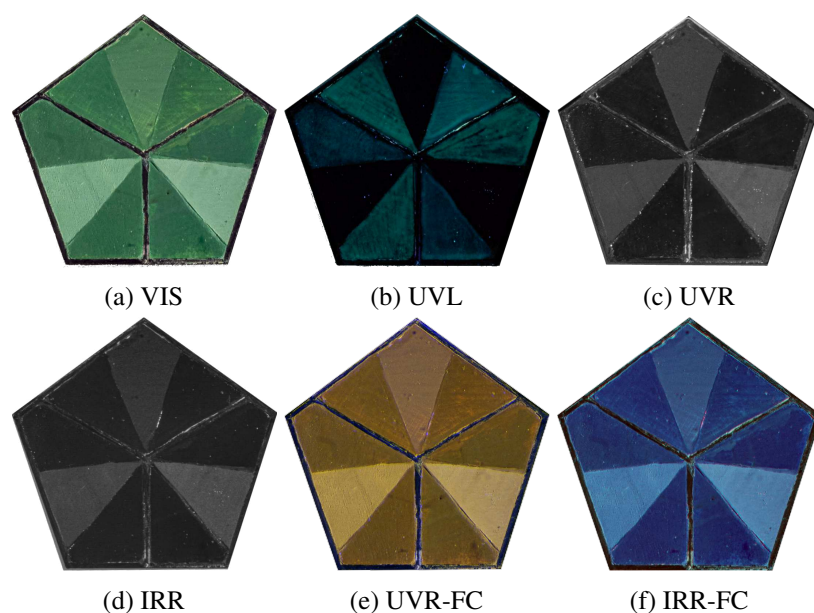
Fig. 7.12 Multispectral images of mock-up with Malachite natural standard.

7.3 Discussion

The multispectral imaging techniques applied to the pictorial preparations allowed the detection of several features.

In particular, the combination of UVR and UVL imaging techniques was successful to identify the varnishes employed and how they were distributed on the surface. Notwithstanding, UVL and UVR imaging were not always successful in the discrimination between the modern and historical varnish. This issue can be due to the fact that both materials used to coat the surface did not undergo any artificial ageing procedure. Indeed, when organic materials as varnishes undergo ageing, they could develop a more intense fluorescent response to UV radiation [55].

In some particular cases, UVL imaging enabled discrimination among the employed binders. For instance, the Lead white, Barium sulphate, and Lapis lazuli pigments when combined with egg tempera, linseed oil, and Arabic gum give a different luminescence colour, as shown in Figure 7.2b, Figure 7.1b, and Figure 7.9b.

In addition, also IRR imaging revealed its potentiality in the detection of underdrawings. Indeed, several pigments are transparent to the IR radiation, such as Lapis lazuli, Lac dye, Minium, Lead-tin yellow, Italian Raw sienna, Lead white, and Barium sulphate. It is interesting to notice that on the areas that have been left

Table 7.1 Pigment employed in the mock-ups and colour assumed in visible images (VIS) and in the ones obtained by infrared (IRR-FC) and ultraviolet (UVR-FC) false colour images processing. Data refers to the layer left unprotected from varnish.

Pigment		Colour		
		VIS	UVR-FC	IRR-FC
Lead white	1, Kr. 46000	white	light pink	white
White barium sulfate	2, Kr. 58700	white	pink	white
Bone black	3, Kr. 47100	black	dark blue	reddish dark
Magnetite black	4, Kr. 48800	black	dark	reddish dark
Raw sienna italian	5, Kr. 40400	brown	purple	brown-green
Lead-tin yellow light	6, Kr. 10100	yellow	orange	white
Minium	7, Kr. 42500	orange	purple	yellow
Lac dye	8, Kr. 36020	red	blue	orange
Lapis lazuli sky-blue	9, Kr. 10562	blue	green	red
Azurite natural fine	10, Kr. 10210	blue	green	purple
Verdigris syntethic	11, Kr. 44450	blue	light green	blue-purple
Malachite natural standard	12, Kr. 10300	green	brown	light blue

uncoated, the underdrawings were more difficult to detect or have not even been identified. This issue could be related to several factors. For instance, the radiation may have been absorbed or reflected differently, on the basis of the presence of the varnish. In addition, the varnishes could have been absorbed by the underlying layers, thus changing the response of the material to the IRR radiation.

Eventually, false colour imaging processing has proven to be a powerful tool to distinguish among pigments that have a similar colour to the naked eye. One example regards the blue pigments, where Lapis lazuli, Azurite, and Verdigris presented a different colour in IRR-FC, which can help the detection on real artworks. Table 7.1 summarises the pigments employed and their response to Infrared-Reflected False Colour (IRR-FC) imaging and UV-Reflected False Colour (UVR-FC) imaging.

Chapter 8

Case Studies

In this chapter, some case studies are presented in which 3D photogrammetry and multispectral imaging were applied as support to multi-analytical diagnostic campaigns.

Some of the work described in this chapter has been previously published in [4].

8.1 Polychrome wooden sculptures from Museo Egizio di Torino

This section presents the analyses carried out on some polychrome wooden models, which belong to the collection of the Museo Egizio di Torino.

This study is performed in the context of a wide conservation project, that involves the investigation of the state of preservation of several Egyptian wooden artefacts and their constituent materials and the study of materials and techniques that could be suitable for conservation treatments. In addition, the characterization of finishes and non-original materials, employed in previous interventions, is performed for the definition of a methodological approach for the conservation treatment.

Fig. 8.1 Image of the wooden artefact form the collection of the Museo Egizio di Torino - Middle Kingdom, beginning of the XXII dynasty (1939-1875 BC).

8.1.1   The artefacts

The artefact object of this study is a wooden sculpture, which portraits a scene of everyday life indoors (Figure 8.1). The model belongs to the collection of the Museo Egizio di Torino and dates back to the Middle Kingdom, at the beginning of the XXII dynasty (1939-1875 BC).

This typology of artefacts is typically part of the funerary ensembles of the Middle Kingdom. They usually consist of three-dimensional models, which aim was to represent common scenes of everyday life. These artefacts had the function of helping the owner of the tomb to get food useful for survival in the afterlife. In addition, they could be cult statues that represented the people working for the owner of the tomb.

The item object of this study is composed of the main element, with a quadrangular shape, that contains other smaller parts. In particular, multiple wooden elements are present on the inside, such as a door, a staircase, and an elevated floor. In addition, several characters are placed within the scene. The wooden models are decorated with a simple palette. It is possible to notice the presence of a carbonate-based preparatory layer and yellow, red, and black pigments.

Regarding the conservation state of the wooden artefact, superficial dust was present on the surface, adhered to a thin film of an acrylic resin spread on the surfaces of the box, and applied in a previous intervention. In addition, it is possible to observe that the surface presents multiple fractures, micro-cracks, widespread

Fig. 8.2 Visible-reflected images of wooden sculpture of sack n°1: front and back view.

Fig. 8.3 Visible-reflected images of wooden sculpture of sack n°2: front and back view.

surface abrasions, and defects in adhesion of the painted film, which results in some de-cohesion of external painted layers.

In this context and in order to assure the conservation of this artefact, among the planned treatments, all the objects had to undergo a cleaning intervention, with the aim of removal of any altered non-original materials.

In particular, three wooden artefacts have been investigated and presented in this dissertation: two sacks, shown in Figure 8.2, and Figure 8.3, and a Scribe sculpture (Figure 8.4).

The performed analyses and the results obtained on the above-mentioned artefacts are presented in the following sections.

Fig. 8.4 Visible-reflected images of wooden sculpture of Scribe: front and back view.

8.1.2 Multispectral 3D model by photogrammetry

It is of fundamental importance to provide the conservators with scientific and diagnostic information that can support the conservation treatments. Among the several analyses that could be carried out, imaging techniques represent a powerful tool for the documentation and investigation of the state of preservation of these artefacts, in a non-invasive and non-destructive way.

In particular, 3D photogrammetry from visible-reflected images can be employed to document the actual state of preservation of the artefacts, with the specific aim of performing monitoring over time. In addition, a multispectral imaging campaign can provide insight into the constituent materials. In addition, MSI techniques can be exploited to map the material discontinuities not detectable with the naked eye and detect the presence of organic materials and substances applied in previous interventions.

Both these techniques have proven to be useful in the Cultural Heritage field. Notwithstanding, considering the aim of this case study, the combined use of these techniques can provide the conservators with a virtual replica of the artefacts, that contain not only the traditional information of geometry and colour of visible photogrammetry but also three-dimensional multispectral data. Therefore the approach presented in this dissertation will be applied to the wooden painted artefacts, to highlight the possible advantages and disadvantages.

In order to reconstruct the multispectral 3D model, the experimental setup presented in Chapter 4 has been employed.

Table 8.1 Parameters employed for the images acquisition of Sack n°1 artefact.

Parameter	Value		
	VIS	**UVL**	**UVR**
Shutter Speed	1s	20s	20s
Acquired images	72 (2x36)	72 (2x36)	72 (2x36)
ISO	200		
Image size	6240x4160		
Image Format	RAW		
Focal Lenght	50 mm		
Aperture	f/16		

Sack wooden sculptures

The sculptures of the sacks present an interesting case study because several deposits are present on the surface. The conservators were interested in detecting the presence of aged materials, both original and belonging to previous treatments, possibly applied to coat and protect the surface or to consolidate the original paint layers.

This typology of organic materials usually presents a fluorescent response and they can be studied exploiting ultraviolet radiation. Indeed, ultraviolet radiation, having a low penetration power, can be used to study the superficial layers, such as varnishes. It is possible to study both the emitted luminescence and the reflected signal, to characterise the distribution of the finishing on the surfaces.

The combination of imaging techniques based on the use of ultraviolet radiation, namely UVL imaging and UVR imaging, and photogrammetry can allow the conservators to map the aged material on the surface and to support the design of the cleaning treatments. In addition, exploiting a UVR-FC 3D model can increase the readability of such information. Therefore, these techniques have been applied to the sculptures of sacks, as described in the following.

Tables 8.1 and 8.2 summarise all the experimental parameters used during the acquisitions, for Sack n°1 and Sack n°2, respectively. In order to obtain the UVR-FC model, the images were processed as described in Section 2.2.4.

Figures 8.5 and 8.6, and Figures 8.7 and 8.8 show a front view and a back view of the 3D virtual replicas of the sculptures of the sack n°1 and n°2, respectively. In

Table 8.2 Parameters employed for the images acquisition of Sack n°2 artefact.

Parameter	Value		
	VIS	**UVL**	**UVR**
Shutter Speed	1s	20s	20s
Acquired images	36	36	36
ISO		200	
Image size		6240x4160	
Image Format		RAW	
Focal Lenght		50 mm	
Aperture		f/16	

particular, the results of a 3D model obtained from VIS, UVL, UVR, and UVR-FC images are presented.

The employed approach enables the identification of several areas in which fluorescent materials are present, for both artefacts. It is possible to notice that, in both sculptures, the surface is covered with a thin layer that responds with a with-ish colour in the UVR-FC model. In addition, several areas are covered in additional materials, probably applied in previous interventions. For instance, in the areas that presented superficial oxidation with less readability of the colours, the UV radiation underlines the presence of a material that resembles a *stucco* layer.

Combining the information coming from both the emitted and reflected UV signal, conservators could deepen their knowledge about the distribution of the materials that have to be removed or consolidated. The 3D model can be easily navigated and consulted during the conservation process, more thoroughly, correlating also three-dimensional geometrical information.
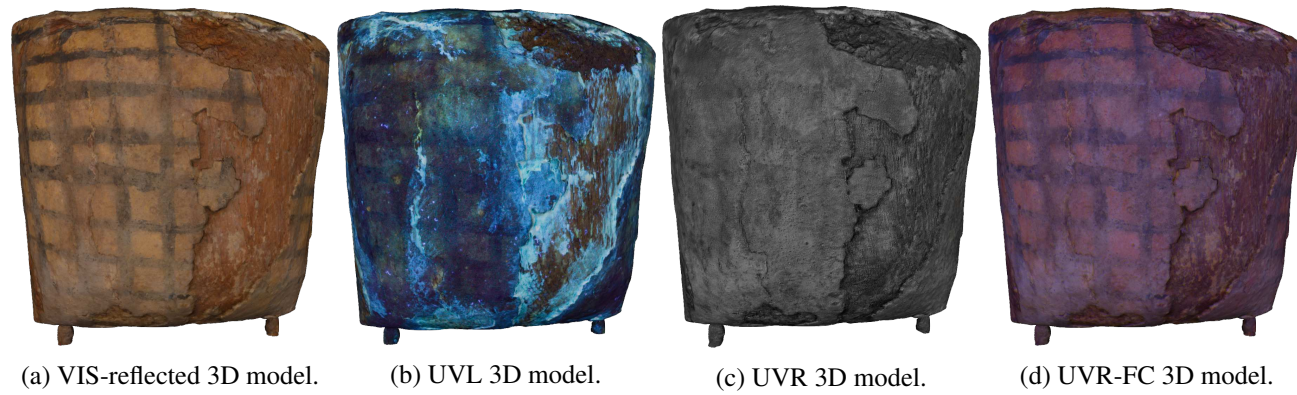
(a) VIS-reflected 3D model.   (b) UVL 3D model.   (c) UVR 3D model.   (d) UVR-FC 3D model.

Fig. 8.5 3D models of wooden sack sculpture n°1 by multispectral photogrammetry, front view.

(a) VIS-reflected 3D model.   (b) UVL 3D model.   (c) UVR 3D model.   (d) UVR-FC 3D model.

Fig. 8.6 3D models of wooden sack sculpture n°1 by multispectral photogrammetry, back view.

(a) VIS-reflected 3D model.   (b) UVL 3D model.   (c) UVR 3D model.   (d) UVR-FC 3D model.

Fig. 8.7 3D models of wooden sack sculpture n°2 by multispectral photogrammetry, front view.

(a) VIS-reflected 3D model.   (b) UVL 3D model.   (c) UVR 3D model.   (d) UVR-FC 3D model.
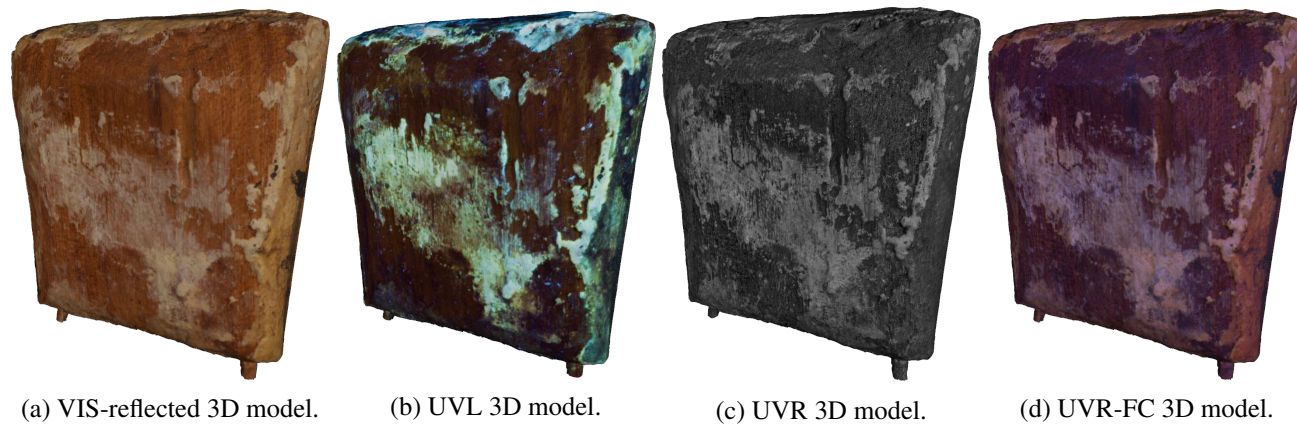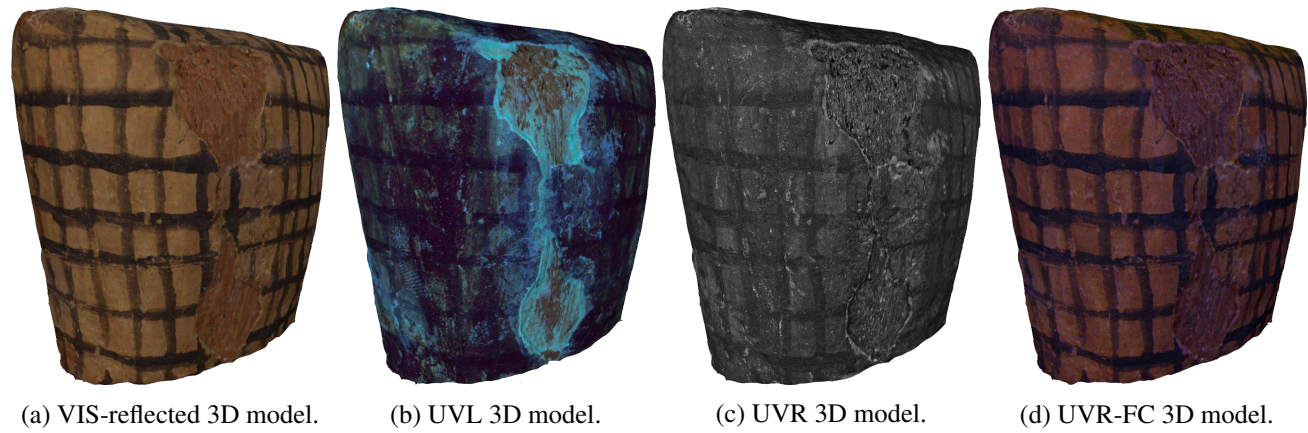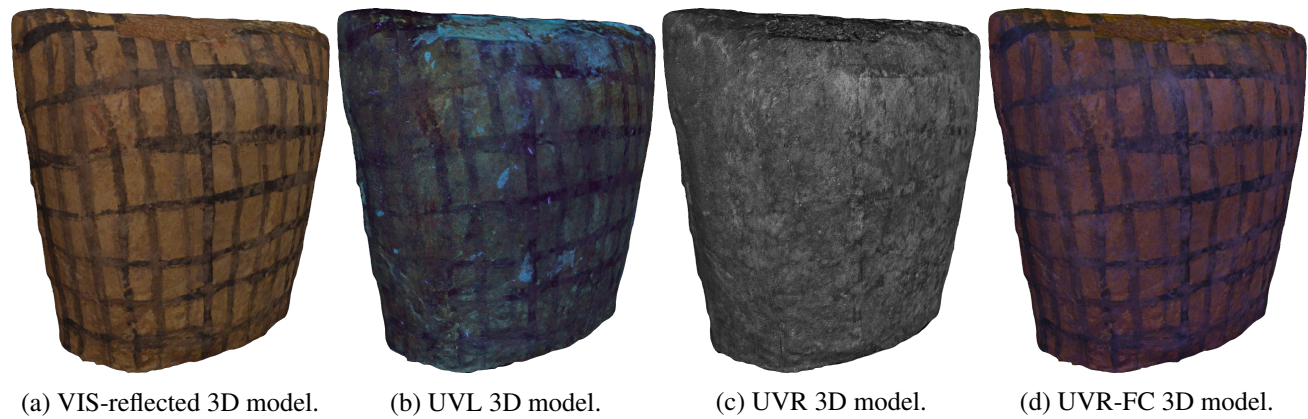
Fig. 8.8 3D models of wooden sack sculpture n°2 by multispectral photogrammetry, back view.

Table 8.3 Parameters employed for the images acquisition of Scribe artefact.

Parameter	Value	
	VIS	**IRR**
Shutter Speed	1s	1/2s
Acquired images	144 (4x36)	144 (4x36)
ISO	200	
Image size	6240x4160	
Image Format	RAW	
Focal Lenght	50 mm	
Aperture	f/16	
Filter	950 nm	

Scribe wooden sculpture

In the specific case of the Scribe sculpture, 3D multispectral imaging techniques have been employed in order to investigate the presence of materials that could have been applied in previous interventions. To this aim, Infrared radiation can help to detect the presence of pictorial materials applied in previous treatments, based on the chemical composition of the investigated material. Indeed, pigments that present a similar colour to the naked eye, could have a different absorbance of the IR radiation.

In particular, Infrared Reflected False Colour Images can be exploited to easily recognise the distribution of the materials on the surface of an artefact. Therefore, this technique has been applied in combination with photogrammetry. Table 8.3 summarises all the experimental parameters used during the acquisitions. To assure coverage of all the surfaces of the artefact, images were acquired setting the artefacts in four different positions, for a total of 144 visible reflected images and 144 Infrared reflected images. In order to obtain the IRR-FC model, the images were processed as described in Section 2.2.4.

Figure 8.9 and 8.10 respectively show a front view and a back view of the 3D virtual replicas of the Scribe sculpture. In particular, the results of a 3D model obtained from visible-reflected images, infrared-reflected images, and infrared reflected false colour images are presented.

This approach can be of significant usefulness for conservators and researchers since it allows for an easy combination of three-dimensional information coming from different wavelengths. Figure 8.11 highlights the presence of some retouches

that have been carried out with a different material with respect to the original one. In particular, it is possible to observe that in visible light the Scribe body has been painted with a reddish uniform pigment. On the other hand, looking at the IRR-FC image it can be seen that the pigment generally acquires a green colour. It is important to notice that in some specific areas, the pigment has a light orange response. This can suggest that some retouching interventions have been made to the surface using a pigment of similar colour in visible light, but with a different chemical composition.

In conclusion, the combination of these techniques can provide an integrated 3D model, useful in the detection of all the previous treatments in a non-invasive way. In addition, based on the pieces of information gathered with this non-invasive approach, further analyses can be planned. For instance few samples could be collected only in the areas of interest, to detect the materials employed for the previous conservation treatments.

(a) VIS-reflected 3D model.   (b) IRR (950 nm) 3D model.   (c) IRR(950 nm)-FC 3D model.

Fig. 8.9 3D models of wooden Scribe sculpture by photogrammetry, front view.

(a) VIS-reflected 3D model.   (b) IRR (950 nm) 3D model.   (c) IRR (950 nm)-FC 3D model.

Fig. 8.10 3D models of wooden Scribe sculpture by photogrammetry, back view.
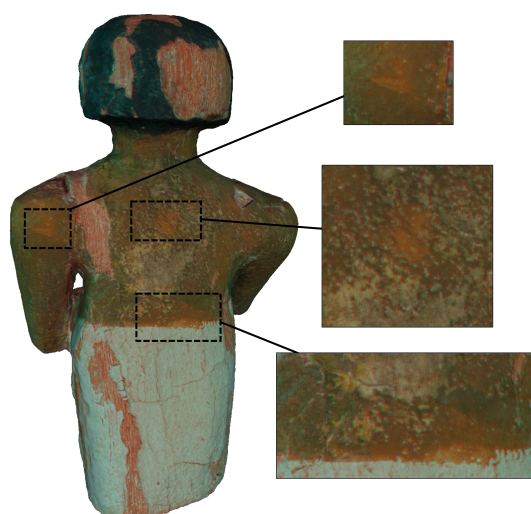
Fig. 8.11 Back view of IRR-FC images obtained on Scribe sculpture. Some previous interventions, that present an orange colour, are highlighted in the image, in black dotted squares.

8.2 Collezione Gori at Fattoria di Celle

In this section "a long-term in-situ monitoring campaign of contemporary bronze statuary exposed outdoor is presented. The case study regards the characterization of three sculptures belonging to the Gori Art Collection, located in the Fattoria di Celle: "Cavaliere" and "Miracolo - Composizione" by Marino Marini and "Due forme o due ombre n°2", by Luciano Minguzzi. The overall conservation state of the sculptures is investigated by means of a multi-analytical and non-invasive approach, involving different techniques. 3D photogrammetry was performed to fully document the artworks. Then, chemical and microstructural features of the corrosion patinas were characterized through X-Ray fluorescence and Raman Spectroscopy. Furthermore, the stability and the protective effectiveness of the corrosion products were assessed by Electrochemical Impedance Spectroscopy. Thanks to the combined use of these specific techniques, the information extracted by the different analyses can be correlated with each other and with the exposure conditions. In particular, the different corrosion products were identified mainly as copper sulphates and phosphates. Eventually, they were correlated to the different microclimate conditions related to their location. The information gathered from the presented multi-analytical approach represents fundamental knowledge in order to develop a tailored conservative project to assure the long-lasting preservation of the artworks"[4].

Fig. 8.12 The investigated artefacts of the Gori Art Collection: "Cavaliere" (left) and "Miracolo - Composizione" (centre) by Marino Marini; "Due forme o due ombre n°2" (right) by Luciano Minguzzi. Figure from [4].

8.2.1 The Artefacts

"The bronze sculptures, subject of the presented study, belong to a private collection of modern art, namely the "Gori Art Collection", located in Fattoria di Celle (Pistoia, Italy). The collection was founded in 1950 in Prato by the two owners, Giuliano and Pina Gori. Many artists contributed with their operas and soon the collection became too large for the original location and thus the artworks had to be moved to a more adequate place. Therefore, in 1970, a new phase started for the collection, which was transferred to the Fattoria di Celle, a large estate situated in Santomato (Pistoia, Italy). The collection kept growing adopting a site-specific art program, in which the sculptures and the multi-materic installations are directly connected to the surrounding parkland and landscape of the Fattoria di Celle, which became an integral part of the collection. Nowadays, it is composed of 80 site-specific artworks and installations created by artists from all over the world [56].

The major part of the pieces belonging to the collection is permanently installed in the gardens of the Fattoria di Celle, in some cases in direct contact with soil or water. The artworks are connected to the space that surrounds them, therefore no protection from the environment is present. As a consequence, many are the corrosion phenomena that can affect these artworks" [4]. "Only some of the bronze artworks understudy will be presented; in particular, the in-situ monitoring of the sculpture "Cavaliere" (Figure 8.12a), created by the Italian artist Marino Marini and

part of the exhibition hosted by the Fondation Maeght in Saint Paul de Vence (France) in 2012 [57, 58]. Marino Marini (1901-1980) is an Italian sculptor, who developed several themes in sculpture: equestrian, divinities, portraits, and circus figures. He drew on traditions of Etruscan and Northern European sculpture in developing these themes. His aim was to develop mythical images by interpreting classical themes in light of modern concerns and techniques. The sculpture under study is part of the collection and it is placed in the garden of the villa, in contact with the soil, in an area surrounded by trees and near to a fountain.

A second sculpture of Marino Marini is object of characterization, the "Miracolo - Composizione" (Figure 8.12b), found by Biancalucia Maglione and confirmed with the Fondazione Marini of Pistoia in December 2015 [58].

The third item of study is "Due forme o due ombre n°2" (Figure 8.12c) by Luciano Minguzzi (1911-2004), an Italian sculptor whose production ranged from a series of vigorously plastic works featuring acrobats, contortionists, and children at play to concentration camps, gas chambers, and other war-related themes.

All the artworks under study are placed in a similar context, on the ground and close to trees and bushes. Even though all the artefacts are of recent realization, there is a lack of information about the materials employed by the artists in their creation. Moreover, information regarding the production techniques is limited too " [4].

8.2.2 Measurement campaign: a multi-analytical approach

"In order to characterize the corrosion processes that are affecting the bronze sculptures, to identify the corrosion products and assess the overall conservation state, an in situ multi-analytical and non-invasive approach was adopted. Indeed, the artworks cannot be moved and techniques that require sampling are not suitable for artefacts with an artistic value.

Firstly, a 3D photogrammetry survey was carried out to create a complete documentation of the artworks. Eventually, chemical and microstructural features of the corrosion patinas were characterised by means of X-Ray fluorescence (XRF) and Raman Spectroscopy (RS). Finally, the conservation state of the bronze sculptures was investigated using Electrochemical Impedance Spectroscopy (EIS) in order to assess the stability and the protective capability of the corrosion patinas grown on the artefact surface" [4].

The employed multi-analytical approach is presented in the following sections.

Photogrammetry

It is worth underlining that the documentation of an artefact is of fundamental importance, most of all if an item is exposed to atmospheric agents that can easily lead to the degradation of the material and thus to the modification of its aspect over time. To this aim, photogrammetry is a suitable technique, since allows to collection and archive of three-dimensional information regarding the colour, geometry, and texture of an artefact. 3D models can be then employed for a variety of useful goals. "One example is the possibility of sharing and communicating art with visual presentations, both for museum and education purposes. Furthermore, a 3D model can be used as a support for restoration or the creation of physical replicas. In addition, digital 3D models can be a resource for cataloging information about the characterization of shape, colour, and texture of artefacts and for supporting diagnostic. These last aspects are the ones stressed in this study. Indeed, photogrammetry was applied as documentation of the conservative state of the sculpture and to store the information regarding the investigated areas" [4].

To create a 3D textured model of the sculpture subject of this study, a low-cost and portable approach was employed. Indeed, photogrammetry can be performed with inexpensive equipment, compared to 3D scanners or laser scanners. In this particular case study, a NIKON D3100 camera and AF-S DX ZOOM-NIKKOR 18- 55 mm f/3.5-5.6G ED lens were employed. In order to create a 3D model, it is important to acquire sharp and clean images, therefore conditions such as focal length, aperture, and exposure time have to be fixed during the entire time of acquisition. Images have to be acquired also at different heights when necessary, to cover all the surfaces of an artefact. Moreover, tools such as a colour chart have to be included within the acquisition scene to assure colour fidelity. In order to obtain the 3D model, the Meshroom software was employed.

Figure 8.13 presents the digital 3D models reconstructed. It is possible to observe that the models are photorealistic virtual replicas of the sculpture's subject of this study.

"An example of how 3D models can be a tool for supporting a monitoring campaign is shown in Figure 8.14. All the information regarding the analysed

Fig. 8.13 3D models by photogrammetry of "Cavaliere" (left), "Miracolo - Composizione" (centre) by Marino Marini, and "Due forme o due ombre n°2" by Luciano Minguzzi (left).

area was organized and integrated into the model itself. Therefore, it became an accessible resource, useful both during the campaign, the data processing, and for sharing knowledge with curators, in a more efficient way with respect to a 2D image. Eventually, this kind of approach can be used also to display the results of the monitoring project, as done in [59–62]. In addition, the final model can be uploaded on online platforms, such as the collection website, with engaging video sequences or as interactive models [63]" [4].

Assessment of corrosion state

In addition, "different and complementary analytical techniques were required in order to acquire an overall characterization of the artefacts and an assessment of their conservation state" [4]. "This is a fundamental aspect for the definition of projects to assure the long-lasting preservation of the artworks. As a matter of fact, the conservation of bronze artefacts exposed outdoor is influenced by the alloy composition, the chemical, microstructural and morphological features of the corrosion products formed on the metallic surface due to the interaction with the atmosphere, as well as by the environmental and microclimate parameters" [4].

Taking into account all these aspects, it was necessary to employ a non-invasive and portable approach.

Fig. 8.14 "Views of the 3D models created for the three artworks. Some of the points of analysis are indicated" [4]. Figure from [4].

In particular, the overall composition of the sculptures was investigated with portable X-ray fluorescence spectroscopy (XRF). This technique allows performing surface elemental analysis. As a matter of fact, XRF is based on the detection of the characteristic X-rays produced from the interaction of the incident beam (an X-ray beam) with the atoms of the investigated material. A Bruker Tracer 5i analyser was employed: this instrument is commercially available and suitable for analysis in the Cultural Heritage field. Indeed it is portable, non-invasive, and non-destructive. "In particular, XRF analyses were carried out both on the "Cavaliere" and "Due forme o due ombre n°2" sculptures" [4].

The corrosion product present on the surface was studied with a chemical technique, the Raman spectroscopy (RS). This technique allows identifying the mineralogical phase present on the surface, through the study of the vibrational modes of the molecules. Also in this case a commercially available instrument was employed: the portable i- Raman Plus by BWTEK. The instrument is equipped with a green excitation laser (532 nm), that is suitable for the detection of the vibrational modes typical of bronze corrosion products. The instrument is also equipped with a spectrometer (BWS465-532S) that works in the range between $150\,\mathrm{cm}^{-1}$ and $4200\,\mathrm{cm}^{-1}$, with a resolution of $7.3\,\mathrm{cm}^{-1}$, and uses a CCD sensor with a cooling system. Raman spectroscopy is a very powerful technique in the Cultural Heritage research field, but in order to extract reliable information, it is important to assess the analytical conditions in order to avoid damaging or modification of the artefact material. Indeed for this case study, different tests were made on artificial corrosion products, in order to identify the most suitable analytical conditions.

Considering the fact that the corrosion phenomena occur through electrochemical reactions, electrochemical techniques are the most suitable for the investigation. One of the often used techniques for the study of the corrosion processes is electrochemical impedance spectroscopy (EIS). It allows for the evaluation of the stability of the corrosion phenomena together with the protective effectiveness of the analysed patina. In order to carry out these measurements, a particular experimental setup was exploited. In particular, a portable electrochemical interface (Ivium-CompactStat.e 10800) was coupled with a measuring probe suitable for non-invasive measurements. The probe was specially developed by the research group of Politecnico di Torino to be suitable for use in the Cultural Heritage field. The probe is designed to be a two-electrode cell. In particular, a Pt wire is used as the counter electrode and the bronze artefact surface as the working electrode. The probe can be attached to the
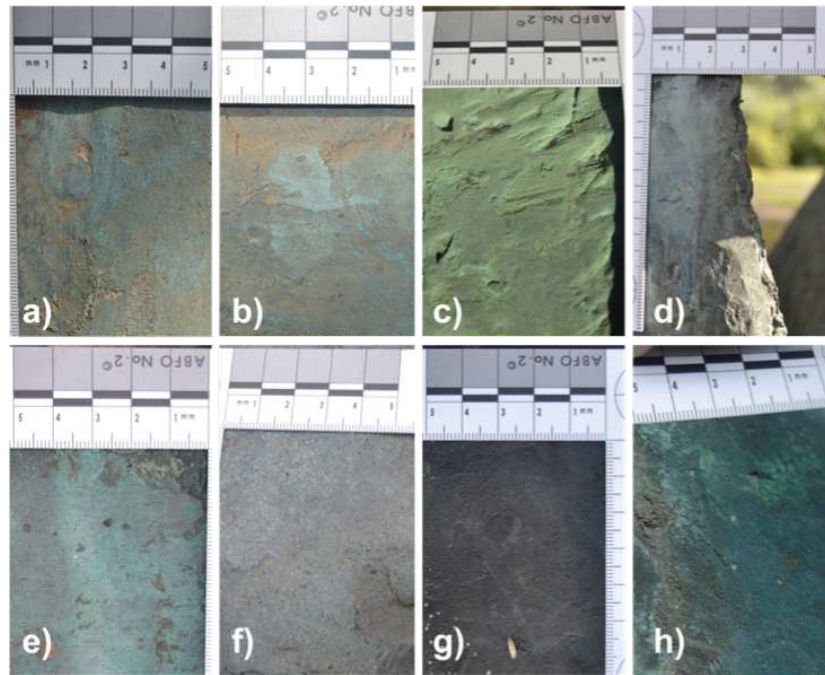
Fig. 8.15 "View of some investigated bronze surfaces. a) DUE_B 01; b) DUE_B 02; c) DUE_U 01; d) DUE_U 03; e) CAV_B 01; f) CAV_U 05; g) CAV_U 07; h) CAV_S 01" [4]. Figure from [4].

artefact through an adhesive polyurethane disc and then easily removed, without damaging the artefact. With this particular configuration, it is possible to perform EIS measurements in situ, directly on the artefact without the necessity of moving the item and without any sampling.

"Different areas of the sculptures were investigated, after a first visual inspection. The areas were selected on the basis of the exposure conditions and colour of the corrosion patina. Some of the corrosion patinas under study are shown in Figure 8.15. As it is possible to observe, black (g), light green (f), light blue-green (a,b, e), bright dark-green (h), green (c) and blue (d) corrosion patinas are present on the sculpture surface. The ones indicated as a), b) and e) were detected on the sculpture's base, while the patinas labelled as c), d), f), g) were mainly found on unsheltered surfaces, as the side of the sculptures. Finally, the area indicated as h) has the characteristic aspect of patinas present in unsheltered parts. Hereinafter, analysis points on the "Cavaliere" sculpture will be labelled as "CAV", on "Miracolo - Composizione" as "MIR" and on "Due forme o due ombre n°2" as "DUE". Then, all measurements will be discriminated according to the position on the artworks: those performed

Table 8.4 "XRF results obtained from "Cavaliere" (indicated as CAV) and "Due forme o due ombre n°2" (indicated as DUE) expressed as counts per second" [4]. Table from [4].

	Cu	Pb	Zn	Sn	Ca	Ni	S	Al	K	Si	P
DUE_U 03	590004	8162	26142	170	-	1888	10	153	-	-	136
DUE_U 02	458367	4236	43790	183	-	824	10	129	-	-	28
DUE_U 01	589645	4598	21856	158	-	1190	10	127	-	-	16
DUE_B 02	506225	8578	45229	213	-	1554	10	89	-	-	98
DUE_B 01	539622	9391	35579	242	-	1709	10	136	-	-	60
CAV_S 10	515908	17757	22252	619	359	366	579	127	-	19	19
CAV_S 09	526733	20171	28701	1244	459	744	531	138	-	28	7
CAV_S 08	523469	12352	29929	1200	384	896	396	127	-	29	20
CAV_S 07	453529	13579	20405	1009	359	425	479	98	-	6	15
CAV_S 06	538036	9741	24153	347	256	460	500	124	-	13	36
CAV_U 03	569577	5159	23296	12	48	596	402	139	20	32	15
CAV_U 02	550258	5252	22204	17	67	568	448	152	33	22	27
CAV_U 01	377554	25165	36945	2655	938	1259	353	96	1	12	52
CAV_B 03	387317	32342	29512	234	533	597	325	111	93	38	57
CAV_B 02	451979	28305	27094	381	509	643	348	142	77	55	83
CAV_B 01	335434	28098	13535	709	523	389	173	93	68	33	30

on the base, will be labelled as "_B", on lateral unsheltered points as "_U" and on sheltered points as "_S". Finally, the single measurement will be identified adding a 2-digit sequential number" [4].

"Thanks to the XRF analysis it was possible to identify all the elements, as shown in Table 1 together with the net intensities obtained with the Bayesian deconvolution. Since it was not possible to use a suitable calibration, due to the presence of the corrosion patina, the performed analysis has to be intended as semi-quantitative. Therefore, the reported quantities have to be interpreted as the relative concentration of elements for each investigated area.

The obtained elements list allows defining the material of all sculptures as bronze composed mainly of Cu, Sn, Pb, and Zn, in accordance with modern bronze composition [64]. The presence of Ca, Si, K, P, and Al can be attributed to soil or environmental contamination.

In order to interpret the large amount of collected data, PCA analysis was performed. The results obtained after the PCA data processing of both sculptures are summarized in Figure 8.16 as biplots with both the loadings and the scores for two selected components (PC1-PC2, PC1-PC3, PC2-PC3) shown in parallel. Data are
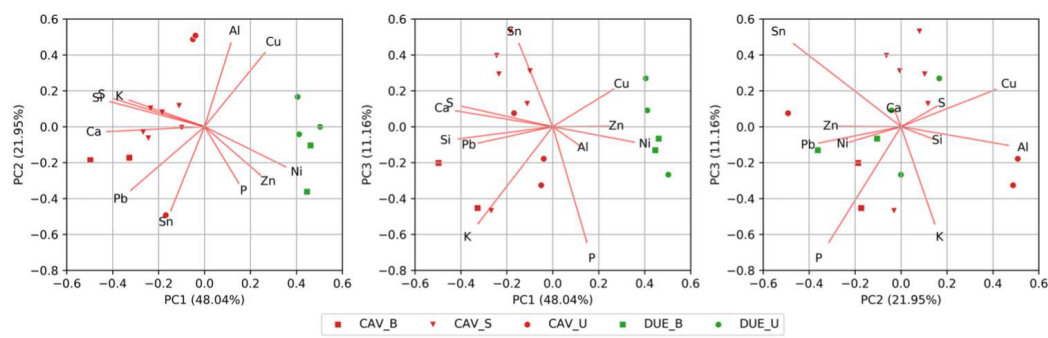
Fig. 8.16 "Score and loading plots of the first three components (PC1-PC2, PC1-PC3 and PC2-PC3) on XRF data" [4]. Figure from [4].

reported with different colours and markers, based on the sculpture and the analysed area. In particular red colour was assigned to the "Cavaliere" work of art, while green to "Due forme o due ombre n°2". Different markers were used to discriminate between the areas where the analysis was performed, as described in the previous section.

As evident from PC1-PC2 plot (Figure 8.16), data are divided into two main clusters, one for each sculpture. This behaviour is mainly due to the PC1 values, positive for the points related to the "Due forme o due ombre n°2" and negative in the other one. This evidence can be related to a major difference in the alloy composition, represented by nickel and zinc content.

Moreover, looking at PC1-PC3 plot it is possible to see that the measurements related to the "Cavaliere" base (CAV_B) are discriminated in a separate cluster from the other ones, suggesting that the base and the sculpture could be made of two different alloys. Indeed, also from a further examination of the "Cavaliere" score points in the PC2-PC3 plot, it is possible to notice that the points of the sculpture base are separated from the other ones and that they present a Pb and P enrichment (the latter presumably due to soil contamination)" [4].

"The identification of the Raman spectra was carried out taking advantage of the information derived from the XRF spectroscopy and by comparison with references from literature [65]. From visual inspection of all the collected spectra, it was possible to identify some recurring patterns typical of copper corrosion products. Given the fact that the surfaces were not cleaned before the analysis, the spectra presented noisy signals (due to fluorescence) and many minor peaks that are not always of easy identification. Moreover, the monitoring campaign resulted in the
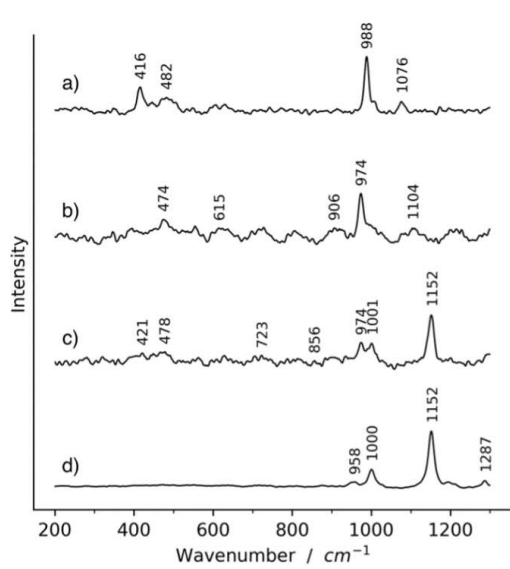
Fig. 8.17 "Representative Raman spectra collected. a) CAV_S 03, antlerite; b) MIR_U 03 brochantite, pseudomalachite; c) CAV_U 03 brochantite, kipushite and silicates, d) DUE_B 01 silicates" [4]. Figure from [4].

collection of a large number of spectra. Therefore, Principal Component Analysis, an unsupervised multivariate analysis, was applied in order to identify the main patterns present in the spectra.

The obtained scores of the three principal components are plotted in Figure 8.18. Data are shown with markers of different shapes and colours. In particular, different colours are assigned to each sculpture (blue for "Miracolo - Composizione", red for "Cavaliere", and green for "Due forme o due ombre n°2"), while different shapes were chosen to represent the category of the investigated area, as previously done.

Looking at the PC1-PC2 plot in Figure 8.18, it is evident that the measurements group in four main clusters. The first group is composed by the "CAV_S" points, having positive PC1 values and negative PC2. The "Miracolo - Composizione" measurements belong to a separate cluster, with PC1 and PC2 positive values. Then a well-defined group is composed of points having negative PC1 and PC2 values, while the remaining points can be grouped as having a positive PC2 value.

In Figure 8.17 a representative spectrum is reported for each of the four groups. The first one (Figure 8.17a, CAV_S) was identified on the basis of the four major bands at 416 cm^{-1}, 482 cm^{-1}, 988 cm^{-1}, 1076 cm^{-1}, that are associated to antlerite, a basic copper sulphate ($Cu_3(OH)_4SO_4$). Dealing with the second one (Figure 8.17b,

Fig. 8.18 "Score plots of the first three components (PC1-PC2, PC1-PC3 and PC2-PC3) calculated from Raman Spectroscopy measurements. Percent variance captured by each PC is reported in parenthesis along each axis" [4]. Figure from [4].

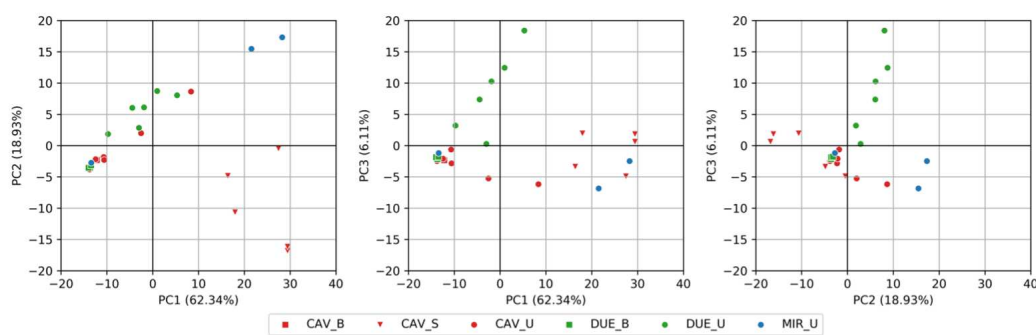MIR_U 03), the major peaks assignments, namely 474 cm^{-1}, 615 cm^{-1}, 906 cm^{-1}, 974 cm^{-1}, 1104 cm^{-1}, allow to identify the brochantite (Cu4SO4(OH)6). Moreover, some of the peaks (974 cm^{-1} and the shoulder at 997 cm^{-1}, 800 cm^{-1} and 605 cm^{-1}) can be related to the presence of copper phosphates like pseudomalachite. The third typology (Figure 8.17c, CAV_U 03) was identified as a mixture of different mineralogical phases. Indeed, the bands at 421 cm^{-1}, 478 cm^{-1}, 974 cm^{-1} can be assigned to brochantite; the 478 cm^{-1}, 723 cm^{-1}, 856 cm^{-1}, 974 cm^{-1}, 1001 cm^{-1} vibration bands are typical of hydroxy-phosphates, in particular they can be assigned to Kipushite (RRUFF ID-R060826 [66]), while the 1152 cm^{-1} is characteristic of the silicates vibration modes [35]. Lastly, the fourth spectrum (Figure 8.17d, DUE_B 01) vibration modes are typical of silicates: 958 cm^{-1}, 1000 cm^{-1}, 1152 cm^{-1}, 1287 cm^{-1} [67].

Given these results, it is possible to confirm the presence of different corrosion mineralogical phases, like copper sulphates, such as brochantite and antlerite and copper phosphate, as kipushite and pseudomalachite (phosphorus presence was also detected by XRF measurements). The presence of silicates was observed, mainly as a contaminant present on the sculpture surfaces. Furthermore, it is possible to correlate the corrosion products to their location and exposure conditions, in accordance with the model proposed by [67–70]. Indeed, in all the analysed areas located on the side of the sculpture, i.e. in rain-exposed surfaces, it is evident the presence of brochantite. This kind of soluble compound can be leached by rains, thus creating a cyclic corrosion mechanism, linked to the frequency with which the surface is exposed to rain. Phase as brochantite can be more stable in sheltered areas, but only

in the 4-6 pH range. As a matter of fact, if the acidity of the water film present on the surface increases and the pH is lowered to values below 4 [65, 69] the precipitation of antlerite is observed. As a matter of fact, antlerite was identified in the areas referred to as "_S", which are all the sculpture sheltered surfaces, where there is a low water evaporation rate" [4].

"Electrochemical Impedance Spectroscopy (EIS) measurements were performed in two different campaigns: the first one in November 2018 and the second one in April 2019. As a matter of fact, EIS is a powerful tool that allows researchers to investigate the corrosion mechanisms affecting metals surfaces and the stability of the superficial oxide and corrosion products layers in a specific environment. So, impedance measurements were performed in order to correlate the chemical composition and morphology of the corrosion products layers to their electrochemical behaviour, and to assess the protective effectiveness of the different corrosion patinas.

The results are summarized in Figure 8.19 as Nyquist plots. Looking at EIS spectra acquired during the November 2018 campaign, it is possible to observe higher impedance values for point CAV_S01, which is in a sheltered position, if compared to points CAV_U04 and CAV_U05, that were in an unsheltered position of the statue. The different electrochemical behaviours can be correlated to the different thicknesses of the patinas, depending on their exposure conditions. Indeed, corrosion products present on unsheltered surfaces are more likely to be washed away by rain, reducing their thickness. It is worth to notice that also using Raman spectroscopy it was possible to similarly discriminate two different behaviours on the basis of the location. As discussed in the previous section, RS experimental findings highlighted the presence of antlerite only in correspondence of sheltered positions, while brochantite is the main corrosion product detected in unsheltered areas. So, correlating the information coming from these two techniques allows to explain the ongoing corrosion mechanism. Actually, patina dissolution in pristine rain is more detrimental in unsheltered areas, where brochantite is present and leads to a decrease in thickness and change in porosity degree. Therefore, in these rain-exposed areas, lower impedance values indicate lower protective effectiveness of the corrosion patina. On the other hand, sheltered areas where antlerite is present, exhibit higher impedance values because patina dissolution by rain is less effective and its thickness is thus higher.
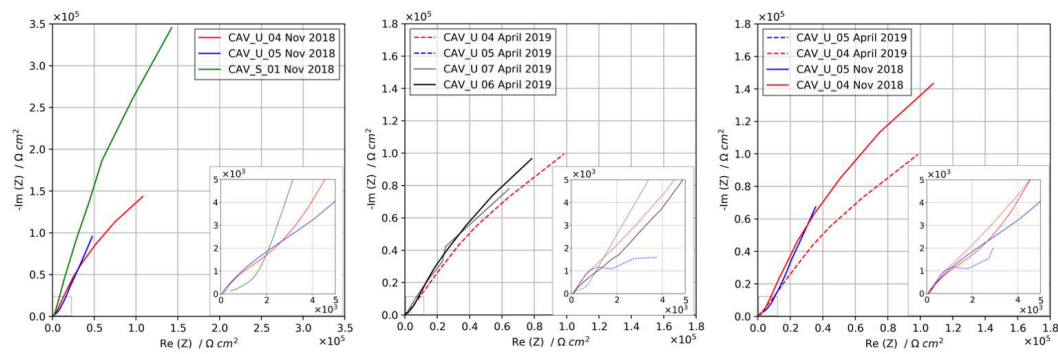
Fig. 8.19 "EIS Nyquist plots recorded on the sculpture "Cavaliere"" [4]. Figure from [4].

The high heterogeneity of the corrosion patinas was further highlighted in the April 2019 campaign. Actually, points CAV_U04, CAV_U06 and CAV_U07 exhibited similar impedance spectra, reaching impedance modulus values in the order of 105 $\Omega \times cm^2$. At the same time, point CAV_U05, which had a behaviour similar to CAV_U04 in the previous campaign, exhibited an impedance modulus more than one order of magnitude lower, confirming the preferential dissolution of brochantite in some positions.

Despite the presence of different behaviours, it is possible to conclude that in all investigated points the patina exhibited good protective effectiveness for the underlying bronze substrate. The relation between the different positions and the corresponding impedance spectrum should be further investigated in order to reach a deeper understanding of the corrosion behaviour of the patinas grown on the different points and the effect of the exposure to environmental conditions" [4].

8.2.3   Conclusions

The approach involving non-invasive analyses performed with several techniques "has proven to be a very interesting and effective methodology for the conservation state assessment of artefacts. This approach could be applied to different case studies, related to multi-materic artefacts, allowing continuous monitoring and documentation of the conservation state of the artefacts. Moreover, the importance of the use of portable instruments lies in the possibility to perform the measurements in situ avoiding any sampling and assessing the degradation of the material directly in contact with the environment to which the artwork is always exposed.

The combination of techniques such as photogrammetry, Raman spectroscopy, X-Ray fluorescence spectroscopy, and electrochemical impedance spectroscopy can be used in order to provide information regarding the overall conservation state of an artefact. Indeed, it allowed to identify which corrosion products are present and to characterise their chemical and microstructural features, together with their electrochemical stability, and to correlate them to the exposure conditions and with the surrounding environment. Moreover, with this approach, it is possible to document all the analysis performed on the artworks and to integrate this information on a virtual 3D model, that can be stored and also shared with curators and conservators.

In particular, it was possible to identify copper sulphates as brochantite and antlerite, and copper phosphate, as kipushite and pseudomalachite. Furthermore, the corrosion products detected were also correlated to their location on the sculptures and their exposure conditions, and the difference between the sheltered and unsheltered surfaces was analysed" [4].

Lastly, the pieces of information gathered with this research approach, "are essential in order to establish tailored preventive conservation strategies. Moreover, the identification of the present corrosion products can help to define if conservation treatments, as cleaning, passivation or coating, are necessary" [4].

Chapter 9

Conclusions

Techniques such as photogrammetry and multispectral imaging are widely diffused in the Cultural Heritage field. Notwithstanding, they provide complementary information, and they are usually separately performed on artefacts. In recent years, the possibility of integrating spatial and radiometric data on a unique model is arising great interest among the experts. These 3D models can serve as documentation tools, as an archive to preserve the artefacts for posterity and safeguard them in case of loss. Therefore, the assessment of the dimensional accuracy of a 3D model, applied in the Cultural heritage field, is an aspect that must be investigated.

In this context, this dissertation presented the design and development of a novel reference object that can be used to assess the dimensional accuracy of 3D models obtained through photogrammetry and that can be employed as a reference for the integration of multispectral data on virtual replicas. The research work on the reference object has been carried out using two approaches, one regarding the metrological characterization and the other one dealing with the acquisition and integration of radiometric data.

The metrological characterization has been performed by comparing the data of the 3D model obtained through photogrammetry with different sets of reference data. These have been collected using different techniques, such as Coordinate Measuring Machine and Laser scanner, that can measure the geometry of an object with different levels of uncertainty. The reconstruction performed by means of photogrammetry was successful and from the comparison, it is possible to state that photogrammetry led to a reliable reconstruction of the reference object.

In addition, the use of different wavelength ranges within the IR radiation for the improvement of 3D models creation has been investigated, to exclude the reflections due to the shiny nature of the varnishes applied on the artefacts surfaces. 3D models were reconstructed selecting different IR wavelength ranges and comparing the results with the traditional approach based on visible images. The comparison led to the conclusion that using IRR images led to the detection of fewer details with respect to the VIS ones, resulting in virtual replicas with a greater number of surface irregularities.

Lastly, Raman spectroscopy has been applied to characterise the materials employed in the pictorial preparations, in order to monitor the material ageing over time.

To the aim of registering both multispectral and geometrical data on a single virtual 3D model, a novel approach has been investigated and presented. This involves the creation of a 3D model from visible reflected images, to obtain geometrical information. Then, textures obtained from several multispectral imaging techniques are integrated into the model itself. The approach led to the creation of a unique 3D model of the reference object, integrating both geometrical and radiometric data within a single coordinate system. This allows not only to characterise the materials present on artefacts but also to study their distribution on the surface. The result allows researchers, conservators,c† and experts in the field to enhance their knowledge regarding an item, being able to visualise information related to the surface, and also the details concealed to the naked eye.

Eventually, the approach presented in this dissertation has then been applied for the study of some artefacts. In particular, some wooden sculptures from the Museo Egizio di Torino have been investigated, exploiting multispectral 3D models in support of the design of cleaning treatments. In addition, photogrammetry has been used for the multi-analytical study of some bronze sculptures of a private art collection, the Collezione Gori at Fattoria di Celle.

Further aspects of this research can be investigated to enhance the application of multispectral 3D digitalization in support of conservation interventions. In particular, the number of pictorial preparations could be increased, testing also several artificial ageing procedures, to deepen the knowledge related to the pigments used in the past and their response to radiations of different wavelengths. In addition, more

multispectral imaging techniques could be integrated into this approach, to cover a greater number of cases that can be found on the artefacts.

References

[1] Joanne Dyer, Giovanni Verri, and John Cupitt. *Multispectral imaging in reflectance and photo-induced luminscence modes: a user manual.* British Museum London, UK:, 2013.

[2] Leila Es Sebar, Sabrina Grassini, Marco Parvis, and Luca Lombardo. A low-cost automatic acquisition system for photogrammetry. In *2021 IEEE International Instrumentation and Measurement Technology Conference (I2MTC)*, pages 1–6, 2021.

[3] Leila Es Sebar, Luca Lombardo, Marco Parvis, Emma Paola Angelini, Alessandro Re, Sabrina Grassini, Alessandro Bovero, and Alessandro Lo Giudice. Metrological validation of a photogrammetry-based technique. In *2022 IEEE International Instrumentation and Measurement Technology Conference (I2MTC 2022)*, (Manuscript submitted for publication).

[4] Leila Es Sebar, Leonardo Iannucci, Caterina Gori, Alessandro Re, Marco Parvis, Emma Angelini, and Sabrina Grassini. In-situ multi-analytical study of ongoing corrosion processes on bronze artworks exposed outdoors. *Acta IMEKO*, 10(1):241–249, 2021.

[5] Fabio Remondino and Sabry El-Hakim. Image-based 3d modelling: a review. *The photogrammetric record*, 21(115):269–291, 2006.

[6] Dimitar Karastoyanov, Nikolay Stoimenov, and Stanislav Gyoshev. Innovative approach for 3d presentation of plane culturally-historical objects by tactile plates for disadvantaged users (low-sighted or visually impaired). In *MATEC Web of Conferences*, volume 292, page 03004. EDP Sciences, 2019.

[7] Pedro Santos, Martin Ritz, Constanze Fuhrmann, and Dieter Fellner. 3d mass digitization: a milestone for archeological documentation. *Virtual Archaeology Review*, 8(16):1–11, 2017.

[8] K Arámbula, HR Siller, Leonardo De Chiffre, CA Rodríguez, and Angela Cantatore. Evaluation of metrology technologies for free form surfaces. *International Journal of Metrology and Quality Engineering*, 3(1):55–62, 2012.

[9] Luisa Vigorelli, Alessandro Re, Laura Guidorzi, Tiziana Cavaleri, Paola Buscaglia, Marco Nervo, Federica Facchetti, Matilde Borla, Sabrina Grassini,

and Alessandro Lo Giudice. X-ray imaging investigation on the gilding technique of an ancient egyptian taweret wooden statuette. *Journal of Imaging*, 7(11):229, 2021.

[10] Antonia Moropoulou, Elisabetta Zendri, Pilar Ortiz, Ekaterini T Delegou, Ioanna Ntoutsi, Eleonora Balliana, Javier Becerra, and Rocío Ortiz. Scanning microscopy techniques as an assessment tool of materials and interventions for the protection of built cultural heritage. *Scanning*, 2019, 2019.

[11] Hrvoje Glavaš, Marijana Hadzima-Nyarko, Ivana Haničar Buljan, and Tomislav Barić. Locating hidden elements in walls of cultural heritage buildings by using infrared thermography. *Buildings*, 9(2):32, 2019.

[12] Michele Russo, Fabio Remondino, and Gabriele Guidi. Principali tecniche e strumenti per il rilievo tridimensionale in ambito archeologico. *Archeologia e calcolatori*, 22:169–198, 2011.

[13] G Bianco, A Gallo, F Bruno, and M Muzzupappa. A comparison between active and passive techniques for underwater 3d applications. *Int. Arch. Photogramm. Remote Sens. Spat. Inf. Sci*, 34:357–363, 2011.

[14] Karl Kraus. *Photogrammetry*. de Gruyter, 2011.

[15] Elizabeth Keats Webb. *Optimising spectral and 3D imaging for cultural heritage documentation using consumer imaging systems*. PhD thesis, University of Brighton, 2020.

[16] M Kholil, I Ismanto, and MN Fu'ad. 3d reconstruction using structure from motion (sfm) algorithm and multi view stereo (mvs) based on computer vision. In *IOP Conference Series: Materials Science and Engineering*, volume 1073, page 012066. IOP Publishing, 2021.

[17] AliceVision. Meshroom - 3d reconstruction software. Available at https://alicevision.org/#meshroom.LastcheckedonNovember (2021/12/02).

[18] Fabio Remondino, Silvio Del Pizzo, Thomas P Kersten, and Salvatore Troisi. Low-cost and open-source solutions for automated image orientation–a critical overview. In *Euro-Mediterranean Conference*, pages 40–54. Springer, 2012.

[19] Isabella Toschi, Alessandro Capra, Livio De Luca, J Angelo Beraldin, et al. On the evaluation of photogrammetric methods for dense 3d surface reconstruction in a metrological context. In *ISPRS Technical Commission V Symposium, WG1*, volume 2, pages 371–378, 2014.

[20] J-Angelo Beraldin, Marc Rioux, Luc Cournoyer, Francois Blais, Michel Picard, and Jim Pekelsky. Traceable 3d imaging metrology. In *Videometrics IX*, volume 6491, page 64910B. International Society for Optics and Photonics, 2007.

[21] J-Angelo Beraldin, Francois Blais, S El-Hakim, Luc Cournoyer, and Michel Picard. Traceable 3d imaging metrology: Evaluation of 3d digitizing techniques in a dedicated metrology laboratory. In *The 8th Conference on Optical*, pages 9–12, 2007.

[22] Higinio Gonzalez-Jorge, Belen Riveiro, Julia Armesto, and Pedro Arias. Verification artifact for photogrammetric measurement systems. *Optical Engineering*, 50(7):073603, 2011.

[23] Costantino Buzi, Ileana Micarelli, Antonio Profico, Jacopo Conti, Roberto Grassetti, Walter Cristiano, Fabio Di Vincenzo, Mary Anne Tafuri, and Giorgio Manzi. Measuring the shape: performance evaluation of a photogrammetry improvement applied to the neanderthal skull saccopastore 1. *Acta Imeko*, 7(3):79–85, 2018.

[24] Anestis Koutsoudis, Blaž Vidmar, George Ioannakis, Fotis Arnaoutoglou, George Pavlidis, and Christodoulos Chamzas. Multi-image 3d reconstruction data evaluation. *Journal of cultural heritage*, 15(1):73–79, 2014.

[25] Alessio Calantropio, Marc Pierrot Deseilligny, Fulvio Rinaudo, and Ewelina Rupnik. Evaluation of photogrammetric block orientation using quality descriptors from statistically filtered tie points. *International Archives of the Photogrammetry, Remote Sensing & Spatial Information Sciences*, 42(2), 2018.

[26] Leila Es Sebar, Luca Lombardo, Marco Parvis, Emma Angelini, Alessandro Re, and Sabrina Grassini. A metrological approach for multispectral photogrammetry. *Acta IMEKO*, 10(4):111–116, December 2021.

[27] Joseph R Lakowicz. *Principles of fluorescence spectroscopy*. Springer, 2006.

[28] Paolo Antonino Maria Triolo. *Manuale pratico di documentazione e diagnostica per immagine per i BB. CC.* Il prato, 2019.

[29] E Keats Webb. Reflected infrared and 3d imaging for object documentation. *Journal of the American Institute for Conservation*, 56(3-4):211–224, 2017.

[30] Efstathios Adamopoulos, Alessandro Bovero, and Fulvio Rinaudo. Image-based metric heritage modeling in the near-infrared spectrum. *Heritage Science*, 8(1):1–12, 2020.

[31] Antonino Cosentino. Identification of pigments by multispectral imaging; a flowchart method. *Heritage Science*, 2(1):1–12, 2014.

[32] Anna Pelagotti, L Pezzati, Alessandro Piva, and Andrea Del Mastio. Multispectral uv fluorescence analysis of painted surfaces. In *2006 14th European Signal Processing Conference*, pages 1–5. IEEE, 2006.

[33] Erica Nocerino, Dirk H Rieke-Zapp, Elisabeth Trinkl, Ralph Rosenbauer, Elisabetta Farella, Daniele Morabito, and Fabio Remondino. Mapping vis and uvl imagery on 3d geometry for non-invasive, non-contact analysis of a vase.

International Archives of the Photogrammetry, Remote Sensing and Spatial Information Sciences, 42:773–780, 2018.

[34] L Fuster-López, M Stols-Witlox, and M Picollo. Uv-vis luminescence imaging techniques. *Técnicas de Imagen de Luminiscencia UV-Vis*, 2020.

[35] Freecad. Available at https://www.freecadweb.org (2021/12/02).

[36] Tiziana Cavaleri, Paola Buscaglia, Simonetta Migliorini, Marco Nervo, Gabriele Piccablotto, Anna Piccirillo, Marco Pisani, Davide Puglisi, Dario Vaudan, and Massimo Zucco. Pictorial materials database: 1200 combinations of pigments, dyes, binders and varnishes designed as a tool for heritage science and conservation. *Applied Physics A*, 123(6):419, 2017.

[37] Kremer pigmente. Available at https://www.kremer-pigmente.com/en (2021/12/02).

[38] Leila Es Sebar, Emma Angelini, Sabrina Grassini, Marco Parvis, and Luca Lombardo. A trustable 3d photogrammetry approach for cultural heritage. In *2020 IEEE International Instrumentation and Measurement Technology Conference (I2MTC 2020)*, pages 1–6, 2020.

[39] Arduino uno. Available at https://store.arduino.cc/arduino-uno-rev3. (28/11/2020).

[40] Cuda, parallel computing platform. Available at https://developer.nvidia.com/cuda-zone. (30/11/2020).

[41] Danny Sims-Waterhouse, Samanta Piano, and Richard Leach. Verification of micro-scale photogrammetry for smooth three-dimensional object measurement. *Measurement Science and Technology*, 28(5):055010, 2017.

[42] Winggs 3d. Available at http://www.wings3d.com (2021/12/02).

[43] Khairulazhar Zainuddin, Halim Setan, and Zulkepli Majid. 3d measurement & modeling using close range laser scanner for reverse engineering application.

[44] Minolta Konica. Non-contact 3d digitizer vivid 910/vi-910: instruction manual. *Avail-able online: http://www.konicaminolta.com/instruments/download/instructionmanual/3d/pdf/vivid-910vi-910instructioneng.pdf*.

[45] Cloudcompare, 3d point cloud and mesh processing software open source project. Available at https://www.danielgm.net/cc/. (28/02/2022).

[46] Martina Corradini, Lavinia de Ferri, and Giulio Pojana. Spectroscopic characterization of commercial pigments for pictorial retouching. *Journal of Raman Spectroscopy*, 52(1):35–58, 2021.

[47] Lucia Burgio and Robin JH Clark. Library of ft-raman spectra of pigments, minerals, pigment media and varnishes, and supplement to existing library of raman spectra of pigments with visible excitation. *Spectrochimica Acta Part A: Molecular and Biomolecular Spectroscopy*, 57(7):1491–1521, 2001.

[48] E Kendix, Giulia Moscardi, Rocco Mazzeo, Pietro Baraldi, Silvia Prati, Edith Joseph, and Simone Capelli. Far infrared and raman spectroscopy analysis of inorganic pigments. *Journal of Raman Spectroscopy: An International Journal for Original Work in all Aspects of Raman Spectroscopy, Including Higher Order Processes, and also Brillouin and Rayleigh Scattering*, 39(8):1104–1112, 2008.

[49] Maria Cristina Caggiani, Antonino Cosentino, and Annarosa Mangone. Pigments checker version 3.0, a handy set for conservation scientists: A free online raman spectra database. *Microchemical Journal*, 129:123–132, 2016.

[50] Eugenia P Tomasini, Emilia B Halac, María Reinoso, Emiliano J Di Liscia, and Marta S Maier. Micro-raman spectroscopy of carbon-based black pigments. *Journal of Raman Spectroscopy*, 43(11):1671–1675, 2012.

[51] Eyasu Mekete, Koen Janssens, and Karolien De Wael. Unraveling the reactivity of minium toward bicarbonate and the role of lead oxides therein. *Analytical chemistry*, 88, 12 2015.

[52] Kui Chen, Kim-Chi Vo-Dinh, Fei Yan, Musundi B Wabuyele, and Tuan Vo-Dinh. Direct identification of alizarin and lac dye on painting fragments using surface-enhanced raman scattering. *Analytica chimica acta*, 569(1-2):234–237, 2006.

[53] Iacopo Osticioli, NFC Mendes, A Nevin, Francisco PSC Gil, M Becucci, and E Castellucci. Analysis of natural and artificial ultramarine blue pigments using laser induced breakdown and pulsed raman spectroscopy, statistical analysis and light microscopy. *Spectrochimica Acta Part A: Molecular and Biomolecular Spectroscopy*, 73(3):525–531, 2009.

[54] Juliana Buse, Vanessa Otero, and Maria J Melo. New insights into synthetic copper greens: the search for specific signatures by raman and infrared spectroscopy for their characterization in medieval artworks. *Heritage*, 2(2):1614–1629, 2019.

[55] Mathieu Thoury, Mady Elias, Jean Marc Frigerio, and Carlos Barthou. Nondestructive varnish identification by ultraviolet fluorescence spectroscopy. *Applied spectroscopy*, 61(12):1275–1282, 2007.

[56] Collezione gori fattoria di celle. Available at http://www.goricoll.it/#.LastcheckedonJanuary (20212/02/17).

[57] L Hegyi, O Kaeppelin, and M Mcphail. Arcadia in celle. *L'Art pour la Nature, la Nature pour l'Art, Maeght Fondation, Saint Paul-de-Vence*, 2012.

[58] Giovanni Carandente. *Marino Marini: catalogo ragionato della scultura*. Skira, 1998.

[59] Fabrizio Ivan Apollonio, Vilma Basilissi, Gabriele Bitelli, Marco Callieri, Dora Catalano, Matteo Dellepiane, Marco Gaiani, Federico Ponchio, Francesca Rizzo, Angelo Raffaele Rubino, et al. Il restauro della fontana del nettuno a bologna. un sistema 3d web per la documentazione e la gestione dei dati. *Archeomatica*, 8(4), 2017.

[60] Andrea Angelini and Damiano Portarena. Advice for archaeological survey with recent technologies. *Acta IMEKO*, 7(3):42–51, 2018.

[61] Maria Cristina VALENTI, Agnese PARRONCHI, Prisca GIOVANNINI, Antonio PAOLUCCI, Cristina ACIDINI LUCHINAT, Simonetta BRAN-DOLINI D'ADDA, and Mauro MATTEINI. *Exploring David: diagnostic tests and state of conservation.* Giunti, Firenze, 2004.

[62] Matteo Dellepiane, Marco Callieri, Massimiliano Corsini, and Roberto Scopigno. Using digital 3d models for study and restoration of cultural heritage artifacts. *Digital imaging for cultural heritage preservation: Analysis, restoration, and reconstruction of ancient artworks*, pages 37–69, 2011.

[63] Elisa Bonacini, Davide Tanasi, and Paolo Trapani. Digital heritage dissemination and the participatory storytelling project# izitravel sicilia: The case of the archaeological museum of syracuse (italy). *Acta Imeko*, 7(3):31–39, 2018.

[64] S Bracci, A Cagnini, Maria Perla Colombini, OA Cuzman, F Fratini, M Galeotti, D Magrini, R Manganelli del Fà, S Porcinai, S Rescic, et al. A multi-analytical approach to monitor three outdoor contemporary artworks at the gori collection (fattoria di celle, santomato, pistoia, italy). *Microchemical Journal*, 124:878–888, 2016.

[65] Ray L Frost. Raman spectroscopy of selected copper minerals of significance in corrosion. *Spectrochimica acta Part A: molecular and biomolecular spectroscopy*, 59(6):1195–1204, 2003.

[66] T Armbruster and RM Danisi. The power of databases: the rruff project. *Highlights in mineralogical crystallography*, pages 1–30, 2015.

[67] Ewen Smith and Geoffrey Dent. *Modern Raman spectroscopy: a practical approach.* John Wiley & Sons, 2019.

[68] Luc Robbiola, Christian Fiaud, and Stéphane Pennec. New model of outdoor bronze corrosion and its implications for conservation. In *ICOM Committee for Conservation tenth triennial meeting*, volume 2, pages 796–802, 1993.

[69] Luc Robbiola and Loïc-P Hurtel. New contribution to the study of corrosion mechanisms of outdoor bronzes: characterization of the corroding surfaces of rodin's bronzes. *Mémoires et Etudes scientifiques Revue de Métallurgie*, 88(12):809–823, 1991.

[70] Valerie Hayez, Joseph Guillaume, Annick Hubin, and Herman Terryn. Micro-raman spectroscopy for the study of corrosion products on copper alloys: setting up of a reference database and studying works of art. *Journal of Raman Spectroscopy*, 35(8-9):732–738, 2004.